Summer 2023

Computational Comparison of Platinum, Base Metals, and Binary Intermetallic Compounds' Efficiency in Hydrogenation Catalysis

Lauren M. Sayler
Missouri State University, lms492s@MissouriState.edu

COMPUTATIONAL COMPARISON OF PLATINUM, BASE METALS, AND BINARY INTERMETALLIC COMPOUNDS' EFFICIENCY IN HYDROGENATION CATALYSIS

A Master's Thesis

Presented to

The Graduate College of

Missouri State University

In Partial Fulfillment

Of the Requirements for the Degree

Master of Science, Chemistry and Biochemistry

By

Lauren Sayler

August 2023

COMPUTATIONAL COMPARISON OF PLATINUM, BASE METALS, AND BINARY INTERMETALLIC COMPOUNDS' EFFICIENCY IN HYDROGENATION CATALYSIS

Chemistry and Biochemistry

Missouri State University, August 2023

Master of Science

Lauren Sayler

ABSTRACT

In the petroleum industry, platinum is used as a catalyst in hydrogenation reactions during petroleum refining. Although platinum is extremely effective as a catalyst, it is expensive. This is an investigation into platinum and what characteristics make it so efficient, with the end goal of finding intermetallic compounds composed of base metals that are as effective in hydrogenation catalysis. The metals used in this investigation are Fe, Co, Ni, Mo, and W. The research performed here is computational and used to support and direct decisions made in the laboratory. The computation is first-principle, which is accomplished using Vienna Ab initio Simulation Packaging (VASP). VASP is used to simulate the adsorption of H_2 and ethylene on the surfaces of Pt, Pd, Fe, Co, Ni, Mo, W, and binary compounds Co_3Mo and Fe_7Mo_6. These simulations allow for the evaluation of adsorption energy, the density of states, and electronic band structures for the metal surfaces and their interactions with the molecular orbitals of H_2 and ethylene. The relationship between these computational results and the catalytic performance of these metals are investigated in order to understand what characteristics in Pt's electronic structure makes it a more effective hydrogenation catalyst. Information gained through the calculations can give insight into which characteristics are desired and could give rise to an intermetallic binary compound that is as effective in hydrogenation catalysts.

KEYWORDS: hydrogenation, adsorption, platinum catalyst, intermetallic compounds, computational chemistry, structural optimization, first principle DFT calculation

COMPUTATIONAL COMPARISON OF PLATINUM, BASE METALS, AND BINARY INTERMETALLIC COMPOUNDS' EFFICIENCY IN HYDROGENATION CATALYSIS

By

Lauren Sayler

A Master's Thesis
Submitted to the Graduate College
Of Missouri State University
In Partial Fulfillment of the Requirements
For the Degree of Master of Science, Chemistry and Biochemistry

August 2023

Approved:

Fei Wang, Ph.D., Thesis Committee Chair

Gary Meints, Ph.D., Committee Member

Gautum Bhattacharyya, Ph.D., Committee Member

Tiglet Besara, Ph.D., Committee Member

Julie Masterson, Ph.D., Dean of the Graduate College

ACKNOWLEDGEMENTS

I would like to acknowledge the ACS Petroleum Research Fund (61754-UR10) which funded this research through Dr. Fei Wang's research group. I am also very grateful to Missouri S&T's Center for High-Performance Computing Research for the use of their supercomputer the Foundry.

I would like to thank the following people for their support during the course of my graduate studies and the completion of my thesis. This endeavor would not have been possible without my advisor Dr. Fei Wang and his help during research and writing. My words cannot express my gratitude to the chair of the department Dr. Wanekaya and my defense committee for their support and feedback throughout this process. I would also like to thank the administrative staff, Linda for all her help solving the numerous problems that came up during my time at MSU.

I am also deeply thankful to my classmates for their encouragement throughout this process and their unending faith in me. I would like to specifically give thanks to Clara for her help in editing during this process. I am also thankful to my family and significant other for their support, without them I could not have finished this thesis.

TABLE OF CONTENTS

LIST OF TABLES

LIST OF FIGURES

INTRODUCTION

The research discussed in this thesis focuses on why platinum(Pt) is more effective as a heterogenous catalyst than other metals in the hydrogenation reactions of olefins (alkenes) compared to base metals and their compounds, which will offer us suggestions in developing more economic base metal hydrogenation catalysts. The base metals investigated are molybdenum(Mo), tungsten(W), cobalt(Co), nickel(Ni), and iron(Fe) as well as two binary intermetallic compounds composed of these base metals, Co_3Mo and Fe_7Mo_6. The primary interest in these metals is the fact that these base metals and their compounds also exhibit catalytic activity in certain hydrogenation reactions and cost much less than Pt.[1] However, none of these base metals by themselves are as effective as Pt in hydrogenation catalysis. Ideally, if two of these metals that are not ideal can be combined to create an intermetallic compound that replicates the electronic structure of Pt then they could replace Pt in catalyzing the hydrogenation of olefins. This idea would lead to a "pseudo-Pt" catalyst using the idea of "like electronic structure, like catalysis" proposed by Tsai.[2] For this purpose, with quantum mechanical computation, I compared the electronic structure of Pt with the electronic structures of the base metals and studied the initial step of heterogeneous catalysis, that is the adsorption of reactant molecules on the metal surfaces, in this case using H_2 and ethylene, since it is the simplest alkene.

Effects on the Petroleum Industry

Finding an efficient substitute for Pt in these reactions is especially beneficial to the petroleum industry since Pt is broadly used in the refining of crude oil into gasoline as well as

other products. In the petroleum industry, crude oil that is drilled from the earth must be refined for it to be in a usable condition. The refinement of oil can produce a multitude of products depending on the process used but the major products are fuels such as gasoline. Gasoline mainly contains medium length carbon chains ranging between C_4 and C_{12} with the most common being C_5 or pentane and the most desired being C_8 or octane.[1] Sometimes when the oil is removed from the earth it is already in these forms, but more often than not they are recovered as either cyclic molecules, short chain carbons, or long chain carbons, making them extremely viscous.

There are three main processes as seen in Figure 1.1 that the oil can go through to be processed into the desired compositions: hydrocracking, reforming, or hydrogenation. Each of these processes utilizes various catalysts in the process, with Pt being preferred. Hydrocracking involves the breaking of long chain carbons such as C_{20+} into smaller chain carbons such as C_4 and C_{12} length chains. The second process, reforming, does the opposite of hydrocracking and takes very short chain carbons such as methane, CH_4, and propane C_2H_6, and combines them to make the same medium chain carbons. The last process, hydrogenation, transforms unsaturated carbon chains into saturated chains by the addition of hydrogen to any double bonds and the removal of other additional elements presence.

Hydrogenation also lowers the number of aromatic hydrocarbons, olefins, and di-olefins. Removal of these compounds helps to avoid the forming of gum which is viscous and blocks further reactions. Generally, hydrogenation takes carbon chains of the appropriate length and makes them more energy dense by maximizing the amount of hydrogen-carbon bonds in each molecule. Of these three processes, the focus of this investigation will be on hydrogenation, because it is an essential step in eliminating unsaturated hydrocarbons, which causes gumming in fuel. Additionally, Pt metal becomes degraded by sulfur and nitrogen containing compounds,

which are often present in crude oil. In any refinement process that utilizes Pt, the compounds need to go through additional cleaning or refining before Pt can potentially be used.[1] Using metals other than Pt can reduce the effect of sulfur and nitrogen containing compounds on the catalyst present. Reducing degradation lowers the number of resources used, making the process more affordable and environmentally conscious.

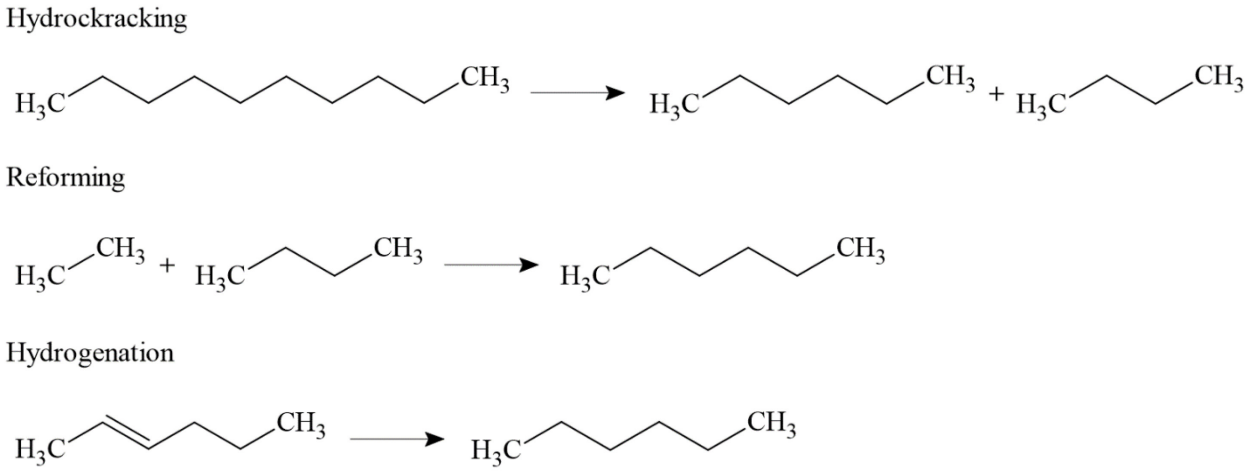

Figure 1.1. Theoretical examples of three types of chemical reactions that occur during oil refinement.

One of the main reasons a replacement for Pt in these processes is desired is due to the cost of Pt being more than six hundred times more than the base metals. In 2020, the petroleum industry was estimated to have used 3,100 kg of Pt which is ninety-three million dollars.[3] The prices for each metal vary depending on the market value but Pt is consistently much more expensive as seen in Table 1.1. So, if a combination of the lower cost metals can be found the cost of oil refining would decrease drastically.

Besides Pt and the base metals mentioned above, Pd is also listed in Table 1.1 because it is often used as a hydrogenation catalyst like Pt. Economically, it is not a base metal and is even

more expensive than Pt. It is included in this study and thesis because of the possibility of characteristics that are similar and produces a desirably efficient catalysis.

Table 1.1. Cost of metals as of May 2023.[4,5]

Metal	Price (dollar/kg)
Pt	$ 31,900
Pd	$41,253
Ni	$21
Fe	$0.113
Co	$30
Mo	$53
W	$25-33

Experimental Background

An experimental evaluation of the base metals' catalytic performance in comparison with Pt was done by Dr. Wang's research group. The experimental backing is attempting to follow the same goal but in an experimental rather than computational format. The computational work of this thesis studied the hydrogenation of ethylene, the simplest alkene, to save computational time and power. However, experimentally, a liquid alkene is practically easier to handle than gaseous ethylene. Therefore, instead of ethylene, experiments focused on the hydrogenation of 1-octene to n-octane in methanol solvent with excess hydrogen at high pressure, around 400 psi H_2. Each

experiment was allowed to run for 24 hours at 60°C before the results were analyzed using gas chromatography, from which the 1-octene to n-octane conversion rate in percentage was obtained and listed in Table 1.2. Compared to the base metals and their intermetallic compounds mentioned above, Pt was by far the most effective in the hydrogenation of 1-octene but Co, Ni, Fe, and Co_3Mo also exhibited some amount of catalytic activity.

Table 1.2. Comparison of hydrogenation using each metal.[6]

Metal	Particle Size (μm)	1-octene	n-octane
Pt	< 3	0.00%	100.00%*
Co	0.5-1.5	15.10%	80.99%*
Ni	2-3	84.39%	15.61%
Fe	5-9	98.32%	1.68%
Mo	2-4	100.00%	0.00%
W	0.6 -0.9	100.00%	0.00%
Fe_7Mo_6	<10	100.00%	0.00%
Co_3Mo	<37	96.22%	3.78%

*Although Co has a high percentage of conversion in reality it required the whole 24 hours to reach this degree of conversion while Pt achieved 100% conversion in much less than 24 hours.

A heterogeneous catalyst's efficiency, besides its chemical identity, is also determined largely by its particle sizes. To evaluate such size effect, in addition to comparing the metals themselves, Pt and Ni with different particle sizes were also tested in the hydrogenation of 1-

octene and the conversion percentages are listed in Table 1.3. Decreasing the particle size increased the conversion rate for both Pt and Ni. Meanwhile, from the Ni at difference sizes, it is also clear that once the particles are smaller than ten μm the catalytic efficiency does not increase significantly upon further decrease in particle size under the adopted experimental conditions. For the base metals compared above in Table 1.2, all particles were smaller than ten μm except for Co_3Mo. This is because Co_3Mo is ductile and difficult to crush into powder. To rectify this ball milling could be attempted to reduce the size below 10 μm and improve its catalytic efficiency.

Table 1.3. Effect of particle size on hydrogenation of 1-octene.

Metal	Particle Size (μm)	1-octene	n-octane
Pt	< 3	0.00%	100.00%
Pt	37-74	94.37%	5.63%
Ni	0.08-0.15	84.07%	15.93%
Ni	2-3	84.39%	15.61%
Ni	3-7	87.54%	11.49%
Ni	37	100.00%	0.00%
Ni	44	92.49%	7.51%

It should be noted that there are more factors that affect heterogeneous catalysts activity, such as surface defects like adatoms, holes, steps etc., as well as which crystalline planes are exposed for catalysis. In this thesis, these factors were not explored. I studied only the most

stable crystalline planes of these metals, which are those with low Miller indices and densest arrangement of atoms, and they were all modeled as perfect crystalline planes without defects.

General Considerations in Computational Chemistry

Based on the experimental results above, a computational evaluation of the metals in question will be pursued. To accomplish this, a program called Vienna Ab initio Simulation Packaging (VASP)[7] was used for all computational calculations. VASP is used for electronic-structure calculations and quantum mechanical molecular dynamics.[8] The calculations are first-principle, utilize density-functional theory (DFT), and employ plane wave functions as the basis functions. From these calculations I can obtain a multitude of information such as surface energy, atomic positions affording the lowest total energy, and electronic band structures, to name a few important to this research.

Additionally, VASP can simulate the adsorption of hydrogen and ethylene on the surfaces of the metals with structural optimization. With these simulations the information given are atomic positions of the molecules on the surface as well as the adsorption energy. After the adsorption, the interaction between the adsorbate's molecular orbitals and the surface metal atoms' atomic orbitals can be analyzed. From all the information obtained through VASP calculations, generalizations can be made about the desirable features of Pt and rationalize how to design a "pseudo-Pt" with only base metals.

Ferromagnetism Vs. Paramagnetism

Three of the base metals being analyzed are ferromagnetic(ferro). This inherent characteristic affects the way interaction occurs between the metal and H_2 or ethylene, since H_2

and ethylene are diamagnetic. Ferromagnetism occurs when a metal has unpaired electrons in *d*-orbitals that are continuously aligned. Paramagnetism also occurs when a metal has unpair electrons in the *d*-orbitals, but the spins are randomly arranged. Both types will respond to a magnetic field, but ferromagnetic compounds are strongly attracted to magnets and are capable of holding that magnetism even after the magnetic field is removed.[9] The ferromagnetic species being analyzed are three metals: Fe, Co, and Ni and the intermetallic compound Co_3Mo. This means when calculations are done for these metals additional parameters must be set for the calculations. To simulate ferromagnetism, the wave functions were calculated separately for the opposite electronic spins, which is called spin polarization. So, two calculations were done for each of these three metals and Co_3Mo, both the non-spin-polarized or paramagnetic (para) and ferromagnetic or spin-polarized, to compare the effects the ferromagnetism has on the adsorption or H_2 and alkenes.

When the paramagnetic calculations are done the results are always hypothetical since each of these metals are ferromagnetic in nature. The comparison of the paramagnetic and the ferromagnetic calculations gives insight into how ferromagnetism affects the electronic structures and the adsorption of H_2 and ethylene. The main effect of ferromagnetism on the calculations is seen in the asymmetric distribution of electrons between the two electronic spins. In most cases, as will be seen later, there are more electrons in one spin (majority spin) and less in the other spin (minority spin). This makes bonding with diamagnetic molecules such as H_2 and ethylene difficult. Because of the additional difficulties it is important to figure out how it affects the hydrogenation reactions.

METHODS

Experimental Design

In order to design a method that allows for the comparison of Pt's electronic structure to those of the base metals and their binary intermetallics, three different scenarios need to be calculated and compared. First, calculations with only the bare surfaces of the metals and binary intermetallics are performed. Second, calculations to simulate the adsorption of H_2 on each surface are performed. Finally, ethylene adsorption is evaluated on the surfaces of each metal or binary compound. These will allow for the comparison between Pt and each metal as well as the intermetallic compounds formed with the base metals.

Two types of information that aid in this comparison are partial charge density (PCD) calculations and density of state (DOS) calculations. PCD calculations allow for the visualization of the valence electron density. This can help visualize the interaction between the *d*-orbitals of the surface layer of metal atoms and the molecular orbitals of ethylene or H_2. The DOS curves are analogous to molecular orbital diagrams and reflect the electronic structures of the metals and intermetallic compounds. Following the principle of "like electronic structure, like catalysis," the high catalytic efficiency of Pt can be rationalized by comparing its DOS with the other metals and binary intermetallics. The DOS can also provide the information to quantitatively evaluate the interactions between the atomic orbitals of the metals and the π orbital of ethylene. For free molecules, ethylene's π electrons are localized within the molecule and their states in the DOS are shown as a sharp peak. As ethylene approaches the surface of the metal slab the π electrons of the ethylene delocalize into the surface and transfer into the metal atomic orbitals, causing the

π peaks within the DOS to broaden. Through the broadening of the peaks, the degree of orbital interaction and π electron transfer can be evaluated.

Procedure

Both PCD and DOS were calculated by VASP. The first step for each calculation was setting up a unit cell. This was done using a program called Visualization for Electronic and Structural Analysis (VESTA) which plots coordinate-based unit cells.[10] VESTA allows for the editing of unit cell dimensions as well as atomic positions. For every VASP calculation, four files are necessary for everything to run properly: POSCAR, INCAR, KPOINTS, and POTCAR.

Creating POSCAR Files. In order to perform calculations, a file containing all of the atomic coordinates and lattice parameters for the unit cell must be created or edited using VESTA. The first step in creating the file was a unit cell of bulk metal, for instance, the fcc unit cell of Pt depicted in Figure 2.1 (a). To simulate a 2-D surface, an isolated "slab" was created from the bulk unit cell. For instance, Figure 2.1 shows the process of making a slab by the stacking of Pt(111) planes. The face centered cubic (fcc) cell (Figure 2.1, a) was firstly transformed into the hexagonal setting (Figure 2.1, b) and then into a 3 × 3 × 4 supercell (Figure 2.1, c). The upper portion of the unit cell was removed to create a slab of atoms spaced from one another by broad gaps. (Figure 2.1, d). The gaps exposed the Pt(111) crystal planes. Once the gap was created, hydrogen or ethylene was placed on the surface. In Figure 2.1, (e), a hydrogen molecule has been placed in the middle of the surface. Structural optimization, which is the optimization of the atomic positions to minimize the total energy, will be performed for the bare metal surfaces (Figure 2.1, d) as well as the hydrogen and ethylene adsorbed on the surface

(Figure 2.1, e). Examples of bulk and slab unit cells for all other metals and binary intermetallic compounds can be found in the appendicies (See Appendix A).

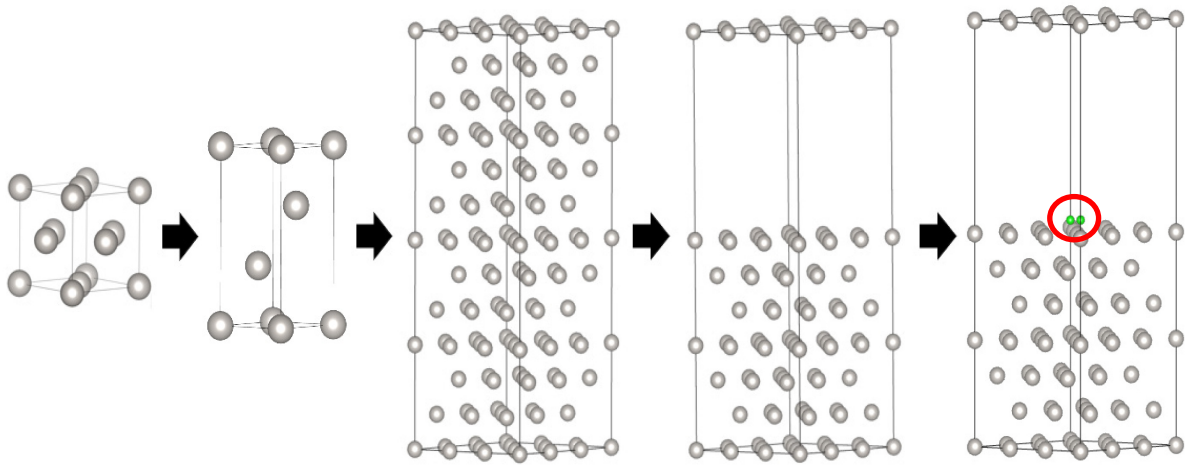

Figure 2.1. Progression of POSCAR file creation from bulk unit cell(a), to hexagonal arrangement(b), to supercell(c), to slab units(d), and to a hydrogen molecule on the surface(e).

Uniformization of Slab Parameters. Before performing all the self-consistent calculations mentioned above with VASP, some computational parameters need to be determined and kept consistent between the various metals and intermetallic slabs, such as the inter-slab distances and the number of layers of atoms whose positions will be optimized. To determine these variables, sets of calculations were performed with Pt using VASP. The inter-slab distance was optimized first. Ideally, it is best to have as short a distance between the slabs as possible since the longer the distance the more computing power and time is required. Calculations were performed on Pt slabs to determine how close the upper slab could be before the calculated total energy is significantly changed. After calculations, a distance of 13.579 Å was adopted for all subsequent calculations.

Two of the more significant parameters that need to be consistent are the thickness of the slab and how many layers of atoms in the slab would be optimized for their atomic positions during structural optimizations. During each calculation, every atom is taken into account and affects the calculation demand and how long it takes. To reduce the computation time, it is optimal to have the smallest unit cell that is physically relevant. On the other hand, it is important that the slab be thick enough so that the inside of the slab can be considered as "bulk"; if the slabs are too thin, all atoms in the slabs will behave as "surface" atoms instead of "bulk."

To test the effects of slab thickness, it was systematically varied between four and eleven layers for Pt slabs. Of all the possible layers, seven layers was chosen because the surface energy, which will be discussed in Chapter 3, for any higher count of layers begins to plateau and any below seven layers had unreasonable adsorption energies compared to the others as can be seen in Figure 2.2. Seven was also chosen because the amount of atoms within the unit cell were reasonable for computing power.

Figure 2.2. Adsorption energy of hydrogen on the surface of Pt slab with variation in slab thicknesses.

Next, the top three layers were optimized during the calculations, which allowed the bottom layers to be held constant and act as "bulk" layers. The three layers were chosen because when performing the calculations to determine the optimal layers the atoms in the cells with seven or more layers showed little movement below the third layer during optimization. The optimization also showed that the surface energy, which will be discussed in Chapter 3, did not change when optimizing below the third layer.

VASP Calculation Paramaters. All calculations were performed using VASP on a cluster computer called The Foundry from Missouri University of Science and Technology. One of the four main files, the INCAR file contains all of the different settings that can be turned on or off depending on what results are desired. The main parameter that was set after performing rounds of calculations was ISIF = 2 which allows for degrees of freedom in the positions of atoms but not the cell shape or the cell volume. Within each calculation the Van der Waal forces were taken into account by using DFT-D3 with zero damping within the function used (IVDW = 11).[11] For all calculations not involving ethylene the precision used was set to "accurate." For ethylene it was set to "normal" because "accurate" calculations involving ethylene adsorption on all surfaces are over-demanding of computational resources. Each calculation initializing the orbitals began from scratch using ISTART = 0. The superposition of the atomic charge densities were taken using ICHARG = 2. Because the first steps of optimization are not reasonable when using random generation of orbitals the first steps are delayed slightly to obtain reasonable orbitals. In this case, the delay occurs in only the first ionic step since NELMDL = -4. The criteria for convergence is dependent on the difference in eV between each electronic loop. In this case the difference I am looking for is 1×10^{-5} eV (EDIFF = 1E-5).

For each calculation four computing cores were used to work on each orbital (NCORE = 4). When performing some of the larger supercell calculations, the automatic limit of 60 electronic steps in the static calculations caused the calculations to finish before completion. As a result, for those larger supercells the electronic steps were set to 120 (NELM = 120). The smearing width was set to 0.1 eV (SIGMA = 0.1) and the partial occupancies for the orbitals are set in optimization to the Methfessel-Paxton scheme (ISMEAR =1). In static calculations, a tetrahedron method with Blöchl corrections set by ISMEAR = -5 is used.[12] The ionic relaxation was done with the conjugate gradient algorithm (IBRION = 2).[13] Additionally, the limit of the number of ionic steps was set to 30 (NSW = 30) and the number of self-consistency steps that are required was 4 (NELMIN = 4). When ferromagnetic calculations were performed for Co, Fe, and Ni two settings are required to specify the spin polarization (ISPIN = 2) and the initial magnetic moment for every atom in the cell which is different for every element (MAGMOM). The magnetic moment is dictated by how many unpaired electrons an atom has, for Co it is 3, for Fe it is 4, and for Ni it is 2. Co_3Mo is ferromagnetic at room temperature while Fe_7Mo_6 is not so, like the ferromagnetic Fe, Co, and Ni, spin-polarized calculations were done for Co_3Mo, too.

KPOINTS and POTCAR Files. Another of the important files necessary for every calculation is the KPOINTS file. This file designates the Monkhorst mesh which dictates the Bloch vectors when the calculation is run. The Monkhorst meshes are dictated by the supercell volume. Since the KPOINTS were dependent on lattice parameters the KPOINTS varied from metal to metal and are listed in Table 2.1. In this case the KPOINTS dictate the reciprocal space in which the cell is found.

The last of the primary files that is required to run the calculation is the POTCAR file. The POTCAR file contains information for each type of atom that will be used in the calculation,

which is the pseudopotential for each element. It gives information such as atomic configuration as well as real wavefunctions and psuedo wavefunctions. The files for each element are generated and provided by VASP.

Table 2.1. The Monkhorst meshes used to sample the first Brillouin zones.

Metal	Monkhorst mesh
Pt (111)	5 × 5 × 1
Pt (011)	3 × 3 × 1
Pt (001)	5 × 5 × 1
Ni	5 × 5 ×1
Pd (111)	5 × 5 × 1
Pd (001)	5 × 5 × 1
Pd (011)	3 × 5 × 1
Mo	5 × 7 × 1
W	5 ×7 × 1
Fe	5 × 7 × 1
Co	5 × 5 × 1
Co_3Mo	3 × 3 × 1
Fe_7Mo_6	7 × 7 × 3

BULK METALS AND METAL SLABS

Comparison of DOS for Bulk Metals and Slabs

Calculations were performed on the bulk metals and their slabs which are shown in Figure 2.1 where the bulk is pictured as (a) and the slabs as (d). Structural optimization was performed on both the bulk and slab structures and the DOS curves can be compared to see whether the metals' electronic structures are significantly altered upon "cutting" the bulk into isolated slabs. The DOS curves for both the bulk and slabs are shown in Figure 3.1 where the colored peaks are the slab and the bolded black peaks are the bulk.

The DOS's for the slabs feature more noise than the bulk DOS. The difference between the two is due to the slabs' computational model structures containing much larger unit cells and more atoms resulting in the calculated DOS having more osillations. Despite these differences, for each metal, its bulk and slab DOS curves are consistent in their overall shapes. This indicates that making the metals into thin slabs does not significantly effect their electronic structures.

In the DOS curves shown in Figure 3.1, the Fermi Level (E_F) divides the occupied states, those below E_F, and the empty states, which are above E_F. The majority of the states, especially the higher DOS peaks, are dominantely contributed to by the *d*-orbitals of the metals. This is made apparent in Figure 3.2 when the DOS of *d*-oribitals are plotted against the total DOS of Pt. This shows that the majority of the states are *d*-orbitals with lesser contributions from the *p*-orbitals or *s*-orbitals.

For heterogeneous catalysis of hydrogenation reactions, the initial step is the adsorption of H_2 and C_2H_4 molecules onto the surface of the metal catalyst. The adsorption is achieved by the donation of the adsorbates' electrons into the empty *d*-orbitals of the surface atoms. Thus, it

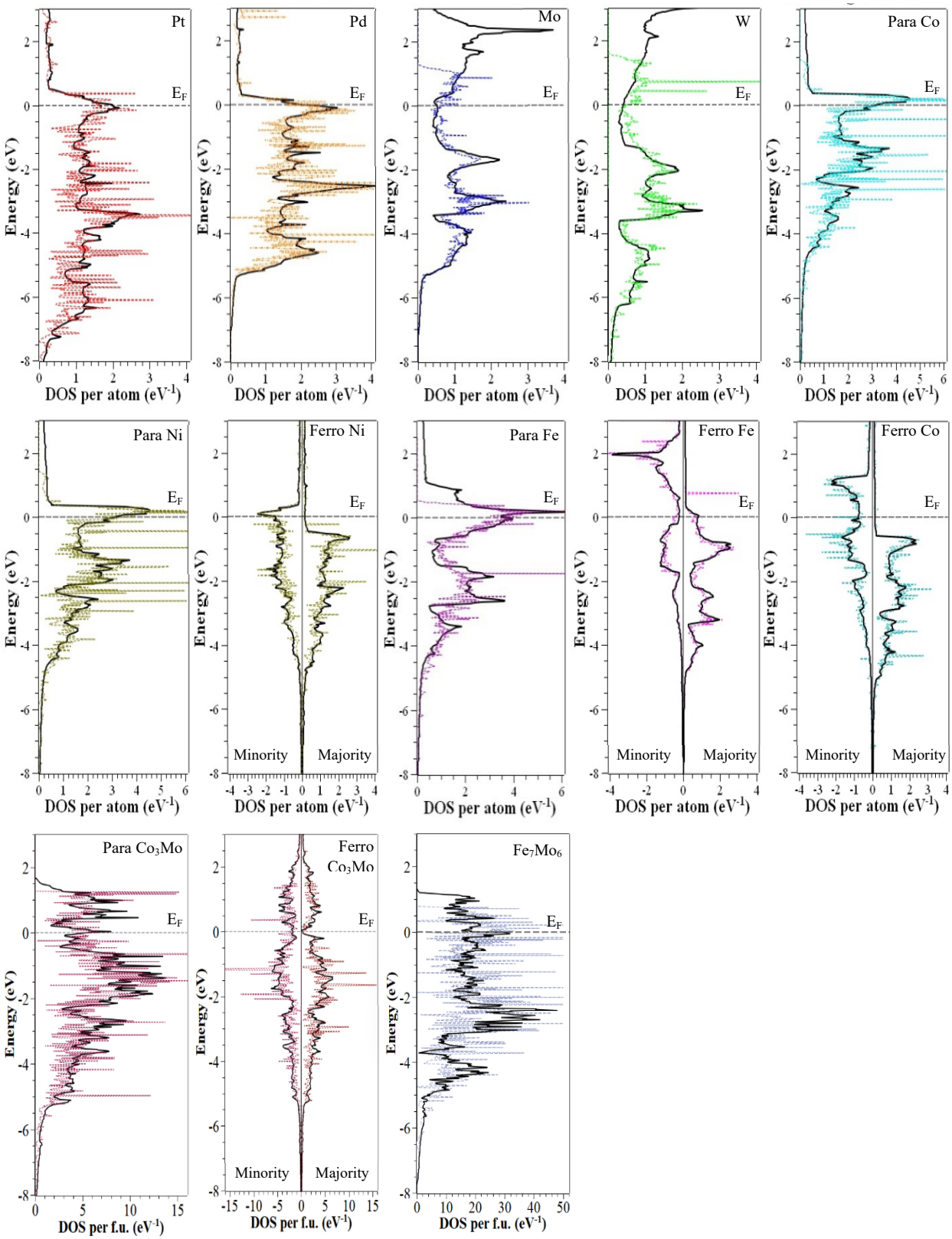

Figure 3.1. Plotted DOS for bulk and slab metals, where the colored data is the slab and the bolded black is the bulk. For the intermetallic surfaces f.u. stands for formula unit.

is desirable for the metal catalyst to have abundant empty states or orbitals just above or at the E_F. Most of these states are low-energy empty *d*-states, which are analogous to the lowest unoccupied molecular orbitals (LUMO), of the metals which can effectively accommodate electrons from the H_2 and C_2H_4 molecules.

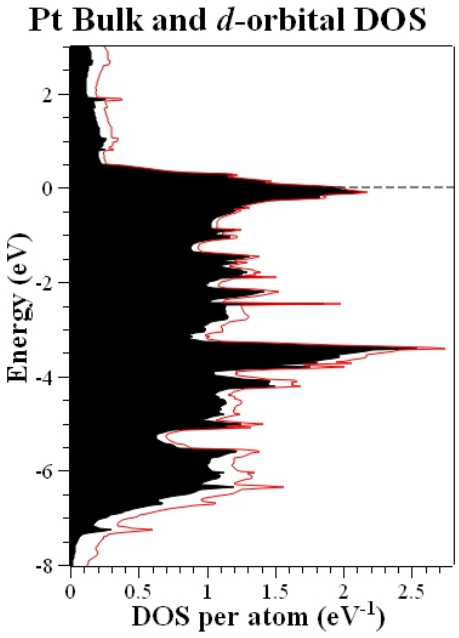

Figure 3.2. Plot of the DOS curve containing only *d*-orbitals in black over the total DOS curve for Pt in red.

For heterogeneous catalysis of hydrogenation reactions, the initial step is the adsorption of H_2 and C_2H_4 molecules onto the surface of the metal catalyst. The adsorption is achieved by the donation of the adsorbate electrons into the empty *d*-orbitals of the surface atoms. Thus, it is desirable for the metal catalyst to have abundant empty states or orbitals just above or at the E_F. Most of these states are low-energy empty *d*-states, which are analogous to the lowest unoccupied molecular orbitals (LUMO), of the metals which can effectively accommodate electrons from the H_2 and C_2H_4 molecules.

It can be seen in Figure 3.1 that Pt's and Pd's E_F are located at a large peak or state-abundant region in DOS. DOS per atom at E_F is 2-3 eV^{-1}. Meaning that Pt and Pd, which are frequently used as hydrogenation catalysts, have very abundant low-energy empty *d*-states at and just above the E_F. Moving to the right, Mo and W both have a large dip, or state deficient region, in DOS around the E_F. The DOS per atom at E_F is lower than 1 eV^{-1}. This means that Mo and W do not have abundant low-energy empty *d*-states to effectively interact with the necessary H_2 and C_2H_4 molecules. This can partly explain why, in the high-pressure hydrogenation of octene in Chapter 1, Mo and W did not exhibit any catalytic activity.

For Fe, Co, and Ni, if I do not apply spin polarization but calculate them as paramagnetic metals, their E_F are also located at state-abundant peaks in their DOS. The DOS per atom at E_F is larger than 4 eV^{-1}, which is even higher than Pt and Pd. However, in the hydrogenation of octene experiments discussed in Chapter 1, Fe, Co, and Ni did not exhibit catalytic activity comparable to Pt. This can be attributed to the fact that these three metals are ferromagnetic metals and their electron spins are polarized. Consequently, in their electronic structure calculations, spin polarization ought to be applied and conduct the ferromagnetic calculations instead of the non-polarized paramagnetic calculations as for the other metals. When spin polarization is on, the DOS for each of the two spins are calculated separately. The ferromagnetic DOS are also shown in Figure 3.1.

The calculated total energy values are compared for the paramagnetic and ferromagnetic calculations for Fe, Co, and Ni in Table 3.1. For each metal the ferromagnetic calculation yields a lower energy, which is consistent with the fact that all three metals are naturally ferromagnetic. Then comparing the paramagnetic verses the ferromagnetic effects on Fe, Ni, and Co, it can be seen that, once ferromagnetic parameters are applied the electronic configuration is vastly

different. In the ferromagnetic calculations, the DOS of the two spins exhibit significant asymmetry. Of the two spins, one spin's DOS peaks are located mostly under the E_F, which is seen on the right side of the DOS curves in Figure 3.1, and the second spin's DOS having a significant portion above the E_F, which appear on the left side of the DOS in Figure 3.1. The asymmetry indicates that there are more electrons in the former spin, or the majority spin, and less in the second spin, or the minority spin. The most important difference from the non-spin polarized DOS is that the E_F is no longer located at state-abundant peaks for both spins with Co and Fe. The DOS is only moderately abundant for the majority spins of Fe and the minority spin of Co. For both cases, the single spin DOS per atom at E_F is about 1 eV^{-1}. For the other spins, the DOS at E_F is much smaller. Ni is similar to Co in that its minority spin features larger DOS around 2.5 eV^{-1} at E_F but the majority spin does not.

Table 3.1. Surface energy per atom of the bulk and slab for the ferromagnetic metals.

Surface	Bulk (eV/atom)	Slab (eV/atom)
Ni_{Para}	-5.80	-5.54
Ni_{Ferro}	-5.86	-5.60
Co_{Para}	-7.11	-6.83
Co_{Ferro}	-7.36	-7.09
Fe_{Para}	-7.96	-7.68
Fe_{Ferro}	-8.52	-8.22

So, these ferromagnetic metals have relatively abundant d-states at and above E_F but only for one spin. This is much less favorable than the DOS of Pt since the surfaces are interacting

with diamagnetic H_2 and ethylene, meaning Fe, Co, and Ni *d*-states must accommodate equal numbers of electrons with both spins, not just the most abundant spin. In order to do so, some of the electrons in the one spin need to "flip" to the other spin. For instance, Ni needs to flip some of its electrons from majority to minority spin to depopulate the majority spin. Once more electrons occupy the minority spin, the *d*-states can effectively accommodate the electrons of both spins in the H_2 and C_2H_4 molecules. This imposes an energy exchange penalty for Fe, Co, and Ni that is not required for adsorption with Pt. This could partly explain why Fe, Co, and Ni exhibited catalytic activity in 1-octene hydrogenation but not as high as Pt.

For the two binary intermetallic compounds, the DOS were calculated not per atom but per formula unit (f.u.), meaning per 4 atoms for Co_3Mo and per 13 atoms for Fe_7Mo_6. This is why the scaling is different and much larger when compared with the other metals. Considering this, Fe_7Mo_6 has relatively high DOS at E_F as does the paramagnetic Co_3Mo. For the ferromagnetic Co_3Mo, the minority spin has higher DOS than its majority spin as which is similar to Co and Ni. Neither of these two binary compounds exhibited high catalytic activity in the experimental hydrogenation of 1-octene. Therefore, abundant empty *d*-states at and directly above the E_F is a desirable feature for the electronic structure but it alone does not guarantee high catalytic performance.

In general, the simulation of the 2-D surfaces through making thin metal slabs did not perceivably alter the electronic structures since the slabs' DOS curves are consistent with those of the bulk metals. From the desired feature of abundant low-energy empty *d*-states for both spins, it can already be partially understood why Pt and Pd are better hydrogenation catalysts than the other metals. This is especially true when comparing Pt to the ferromagnetic metals.

Comparison of Calculated and Experimental Surface Energies

When performing these calcuations it is necessary to evaluate their reliability by comparing calculation results with experimental outcomes. A comparison can be directly made between the calculated surface energy and experimental values from literature. To calculate the surface energy, the method introduced by Ungerer et.al. was adopted and used for Equations 4.1 and 4.2.[14] Using Pt as an example, the total energy was calculated for the bulk Pt ($E_{Pt,bulk}$), the unrelaxed or unoptimized slabs ($E_{slab,u}$), and the relaxed or optimized slab ($E_{slab,r}$). The surface energy for the unrelaxed slabs (γ_u) and eventually the relaxed slabs (γ_r) can be calculated using the following equations. Additionally, A_{slab} is the surface area of the slab and $N_{Pt,slab}$ is the number of atoms in the slab.

$$\gamma_u = \frac{E_{slab,u} - N_{Pt,slab}E_{Pt,bulk}}{2A_{slab}} \qquad \text{Equation 4.1}$$

$$\gamma_r = \frac{E_{slab,r} - N_{Pt,slab}E_{Pt,bulk}}{A_{slab}} - \gamma_u \qquad \text{Equation 4.2}$$

Based on the calculated energy of the relaxed surfaces (γ_r) a comparision can be made with experimental literature and the percent error calculated as seen in Table 3.2. The majority of the surfaces were found to have percent error of less than 15% with molybdenum being the exception with a 20% error. The data also shows platinum as being the most consisent with the experimental literature values with only a 1.2% error. Considering all of the approximations employed by the DFT calculations through VASP, these discrepancies between calculated and experimental surface energies are “acceptable” and works better for some metals than for other metals.

Table 3.2. Comparison between computational and experimental values for surface energy of metals.

Metal	Computed (J/m^2)		Experimental Literature (J/m^2)[15]	Percent error
	γ_u	γ_r		
Pt (111)	2.47	2.45	2.48	1.2%
$Ni(111)_{Para}$	2.22	2.17	2.45	11.5%
$Ni(111)_{Ferro}$	2.17	2.12	2.45	13.4%
Pd (111)	2.15	2.14	2.05	4.6%
$Fe(110)_{Para}$	3.20	2.22	2.48	10.4%
$Fe(110)_{Ferro}$	2.94	2.84	2.48	14.5%
W(110)	4.25	4.15	3.68	12.9%
Mo(110)	3.70	3.57	3.00	19.0%
$Co(001)_{Para}$	3.14	2.63	2.55	3.0%
$Co(001)_{Ferro}$	2.80	2.69	2.55	5.4%

HYDROGEN ADSORPTION

Hydrogen-Hydrogen Bond Lengths

After the optimization of the metal and intermetallic slabs, H_2 molecules were placed on the slab surfaces, followed by atomic position optimization to simulate the adsorption of H_2 onto the surfaces. The same optimization parameters used for the slab were used for all calculations involving H_2 and ethylene. For instance, H_2 was placed on the surface of Pt(111) slab created in Figure 3.1 (d and e), and the initial H─H bond distance is 0.74 Å, which is the accepted distance between hydrogen atoms in H_2.[16] The initial positions of the H_2 molecule can be seen in Figure 4.1. After multiple rounds of optimization, the hydrogen molecule can be seen in Figure 4.1 as the final where the H_2 atoms are now 2.04 Å apart. At that distance, it can be assumed that the H─H bond has been broken since the distance is more than double the covalent bond distance expected between two hydrogens.

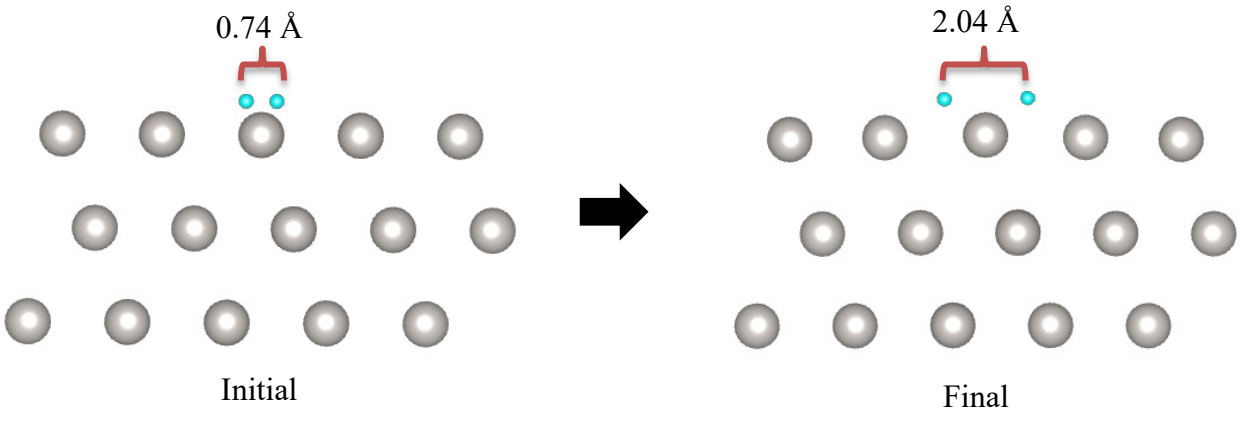

Figure 4.1. Adsorption of H_2 on the surface of Pt.

These calculations for H_2 adsorption were performed on all the metal and intermetallic surfaces calculated in Chapter 3. These metals and intermetallics exhibit varying effects on the distance between the H_2 atoms upon adsorption. Images of adsorbed hydrogen on each surface can be found in Appendix A. The adsorbed H_2 distances can be seen in Table 4.1.

Table 4.1. Distances of H_2 after adsorption on the metal surfaces.

Surface	Å
Pt (111)	2.04
Pd (111)	1.92
W(110)	1.76
Mo(110)	1.79
$Ni(111)_{Para}$	1.83
$Ni(111)_{Ferro}$	1.83
$Fe(110)_{Ferro}$	3.05
$Co(001)_{Para}$	1.82
$Co(001)_{Ferro}$	1.83
$Fe_7Mo_6(001)$	2.82
$Co_3Mo(001)_{Para}$	1.70
$Co_3Mo(001)_{Ferro}$	1.71

Although there is variance in the distance between the H_2 atoms for each metal, the most important conclusion is that in each case the H─H bond has been broken since each distance is significantly longer than the original 0.74 Å. This leads to the conclusion that each metal or binary compound is able to adsorb H_2 onto the surface and break the H─H bond. The actual

distance produced varies due to strength of adsorption as well as the size of the metal atoms. The stronger the adsorption is and the larger the metal atoms are, the longer the H─H distance will be. H atoms may have also diffused on the slab surfaces during the optimization, which can explain the long distances observed for the Fe(110) and Mo(110) surfaces as well as the Fe_7Mo_6 (001) surface. Additionally, there is not a significant difference between the paramagnetic and ferromagnetic substances as seen with the Ni, Fe, Co, and binary compounds.

Adsorption Energies

For each metal surface, the adsorption energy was calculated by comparing the optimized bare slab total energy, calculated in Chapter 4, plus the energy of free H_2 ($E_{slab,r} + E_{H2}$) with the total energy after the adsorption of the H_2 molecule ($E_{slab,H2}$) onto the slab surface as in Equation 4.1. The energy of free H_2 was calculated following the same parameters as all other calculations and was found to be -6.69 eV.

$$E_{ads} = E_{slab,H_2} - (E_{slab} + E_{H_2}) \qquad \text{Equation 4.1}$$

For the data shown in Table 4.2, the more negative the adsorption energy is, the stronger and thermodynamically more stable the H_2 adsorption. The most negative adsorption energy found was Ni(111) with paramagnetic calculations. However, this highly negative value is only "hypothetical" because in reality Ni is a ferromagnetic substance. This "hypothetical" nature is also true for $Co(001)_{para}$ and $Co_3Mo(001)_{para}$. The comparison between these hypothetical paramagnetic calculations and real ferromagnetic calculations is further discussed in the next section.

Table 4.2. Calculated adsorption energy of H_2 on the surface of metals and binary compounds.

Surface	$E_{slab,H2}$ (eV)	E_{slab} (eV)	$E_{slab}+E_{H2}$ (eV)	E_{ads} (eV)
Pt (111)	-421.89	-413.42	-420.12	-1.77
Pd (111)	-356.75	-349.22	-355.92	-0.84
W(110)	-741.41	-733.40	-740.09	-1.32
Mo(110)	-625.11	-617.04	-623.73	-1.38
$Ni(111)_{Para}$	-357.90	-349.24	-355.93	-1.97
$Ni(111)_{Ferro}$	-361.44	-353.11	-359.80	-1.64
$Fe(110)_{Ferro}$	-468.93	-460.59	-467.28	-1.65
$Co(001)_{Para}$	-438.13	-430.07	-436.76	-1.37
$Co(001)_{Ferro}$	-454.77	-446.88	-453.58	-1.19
$Fe_7Mo_6(001)$	-484.10	-475.80	-482.49	-1.77
$Co_3Mo(001)_{Para}$	-921.88	-914.04	-920.74	-1.14
$Co_3Mo(001)_{Ferro}$	-921.20	-915.51	-922.20	1.00

Except for those hypothetical paramagnetic calculations, comparison leads to the conclusion that Pt affords the most stable adsorption of H_2 since it has the most negative value among the remaining adsorption energies. However, there is no apparent correlation between $E_{ads,H2}$ and catalytic performance. For instance, Pd, another common hydrogenation catalyst, has a less negative $E_{ads,H2}$ than every non-ferromagnetic metal or intermetallic compounds, such as Mo, W, and Fe_7Mo_6 which did not exhibit catalysis in the hydrogenation of octene. The lack of correlation can be examined from three different perspectives. The first is that $E_{ads,H2}$ directly quantifies the thermodynamic stability of H_2 adsorption on the metal surfaces, but not the kinetic behaviors of the adsorbate atoms, such as adsorption and desorption rates as well as migration

rates. Secondly, all metals and intermetallics, except for Co_3Mo, feature negative $E_{ads,H2}$ meaning that thermodynamically, H_2 can stably adsorb onto all of their surfaces. This is consistent in the observation of the H─H distances after adsorption that all metals and intermetallics are able to adsorb H_2 and break H─H bonds. Thirdly, the less negative $E_{ads,H2}$ of Pd can be attributed to the fact that H atoms can be "dissolved" into the Pd slab instead of adsorbed onto the surface. This did occur once during structural optimization and is discussed in more detail in a later section.

Paramagnetic and Ferromagnetic effects. The effect of spin polarization on $E_{ads,H2}$ was evaluated for the ferromagnetic metals and intermetallics by comparing the paramagnetic or non-spin-polarized and ferromagnetic or spin-polarized $E_{ads,H2}$, except for Fe. The paramagnetic Fe was excluded due to the calculation results yielding unstable H_2 adsorption as well as unphysical atomic positions. For the other ferromagnetic species, Co, Ni, and Co_3Mo, the $E_{ads,H2}$ were significantly affected by the spin polarization. As seen in Table 4.2 for each of the ferromagnetic species, the paramagnetic $E_{ads,H2}$ is significantly more negative than its ferromagnetic $E_{ads,H2}$. In fact, Co's and Ni's paramagnetic $E_{ads,H2}$ are even more negative than Pt, indicating a more favorable adsorption of H_2, which is unrealistic since Co and Ni are ferromagnetic not para. This echoes the finding in Chapter 4 with the DOS comparison. The hypothetical paramagnetism yields abundant low-energy *d*-states in Chapter 4 and more negative $E_{ads,H2}$ in this chapter. Both of these features indicate better adsorption. Therefore, if the ferromagnetic metals had been para, they would be better adsorbers than Pt.

Palladium anomaly. Another anomaly seen in Table 4.2 is with Pd whose $E_{ads,H2}$ is only -0.81 eV, while all of the others are at least -1.1 or more negative. There could be multiple factors adding to this, but it could be partially due to the fact that Pd can form palladium hydride. The Pd absorbs the H_2 within the interstitial sites of the metal lattice rather than bonding with H_2

on the surface of the metal.[17] One calculation resulted in this absorption of H_2 in the interstitial sites as shown in Figure 4.2 where one H_2 moved below the upper surface of the Pd slab. This result was not used and since it is not relevant to the research being pursued.

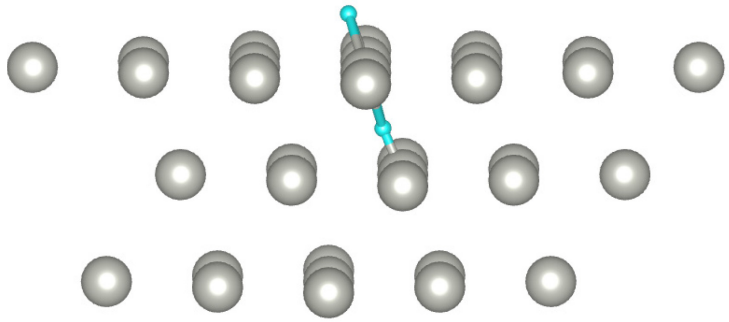

Figure 4.2. The absorption of H_2 into Pd slab interstitial sites.

ETHYLENE ADSORPTION

Optimization of Ethylene

The next step in the research process was to simulate the adsorption of a C═C double bond onto the surface of the various metals and binary intermetallics in question. During the hydrogenation mentioned in Chapter 1, 1-octene was used, but for computational purposes octene as a molecule is too large and demands excessive computational resources in first-principle surface adsorption simulation. So instead, ethylene was used because it is the shortest carbon chain containing a C═C double bond. Limiting the carbon chain length simplifies the calculations as much as possible and decreases the computational time required.

Adsorption Effects on Geometry and Energy

When looking at the adsorption of ethylene on the surface, the main indicator of complete adsorption is the partial breaking of the π-bond in the C═C double bond, which results in a geometry change to the ethylene molecule. Figure 5.1(a) compares the geometry of ethylene and ethane molecules. A free molecule of ethylene is planar and the C═C bond distance is 1.339 Å. If the C═C bond is completely broken the bond transforms into a C─C single bond as seen for ethane where the geometry is non-planar, and the C─C bond becomes longer at 1.535 Å.

The simulation of ethylene adsorption onto Pt(111) surface is shown in Figure 5.1(b). When ethylene is initially placed on the surface, the geometry is planar. After structural optimization, the geometry has altered to become more similar to ethane with non-planar geometry. With the adjustment in geometry also came the lengthening of the C─C bond from 1.339 Å to 1.491 Å, which is still shorter than ethane's 1.535 Å. The change in geometry and

bond length indicates that the structural optimization successfully simulated the adsorption of the ethylene on the surface of the Pt through the partial breaking of the π bond in the C═C double bond. Similar results were also observed with ethylene on the surfaces of other metals and intermetallic compounds. Additionally, besides the partial breaking of the π bond, the orientation of the ethylene also changed (Figure 5.1(b)) so that the C atoms became aligned with and closer to their nearest neighboring Pt atoms, which is due to the formation of bonds between them.

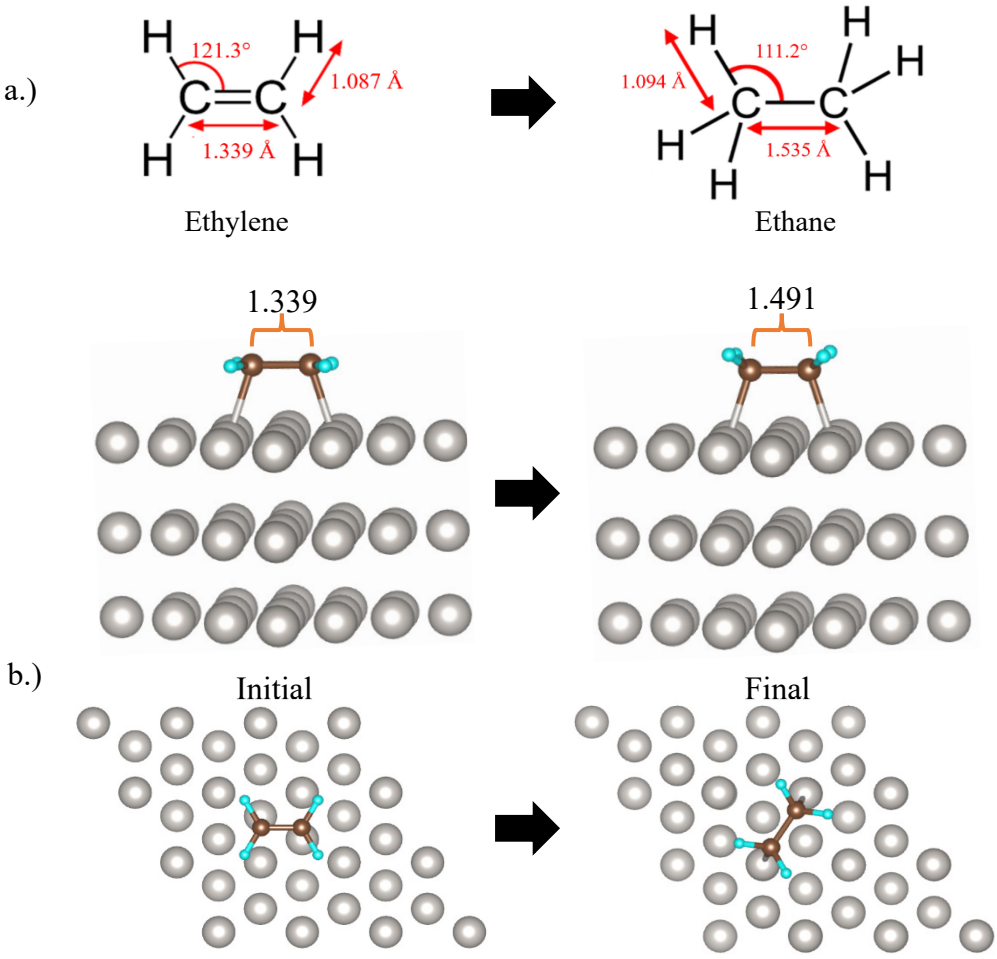

Figure 5.1. Optimization of ethylene on Pt slab, (a) is the structural representation of ethylene and ethane and (b) are the initial and final images from VESTA of ethylene's adsorption onto Pt.[18,19]

Once optimization is completed for all surfaces, the adsorption energies can then be calculated using Equation 5.1. The energy of free ethylene (E_{C2H4}) has the value of -31.98 eV. The results of the calculations can be seen in Table 5.1. Again, the most optimal adsorption energy is the most negative $E_{ads,C2H4}$. As was seen with the H_2, Pt appears to have the most negative adsorption energy. So, Pt is the most effective of the metals in adsorbing both H_2 and ethylene.

$$E_{ads} = E_{slab,C2H4} - (E_{slab} + E_{C2H4}) \qquad \text{Equation 5.1}$$

It is also helpful to compare ethylene's adsorption distances, the distances from ethylene's C atoms to the surface layer of metal atoms after structural optimization is finished. It shows that, even though Pt features the most stable adsorption in terms of $E_{ads,C2H4}$, ethylene is adsorbed at a distance of 2.83 Å away from Pt surface, which is longer than all the other metals and intermetallics. This distance is affected by the metal atoms' sizes but not the atomic sizes alone. W is larger than Pt, but ethylene is much closer, at 2.25 Å, to the W surface when adsorbed. Pt's long adsorption distance is desirable as it will likely allow a faster adsorption of reactants as well as desorption of products. The ethylene-surface distances will be discussed in more detail later in the progressive approaching of ethylene to the surfaces.

Another indication of the effectiveness of adsorption is the C─C bond length in the adsorbed ethylene molecule. The C═C bond length of ethylene is 1.339 Å and the C─C bond length of ethane is 1.535 Å as shown in Figure 5.1 (a). Subsequently, when these two bond lengths are compared to the adsorbed ethylene C─C bond lengths in Table 5.2, the bond has lengthened and is somewhere between the length of a double bond in ethylene and a single bond

in ethane. This indicates that the π-bond from the C═C double bond is partially broken and the π-electrons in the ethylene have been delocalized onto the surface metal atoms. For every metal and binary intermetallic tested, the carbon length was long enough to indicate the partial π-bond breaking. However, unlike $E_{adsC2H4}$, the C─C distance cannot be used quantitatively to determine the effectiveness of adsorption because the sizes and arrangement of surface metal atoms also affect the length of the C─C bond to an unknown extent.

Table 5.1. Calculated adsorption energy and adsorption distances of C_2H_4 on the surface of metals and binary compounds.

Surface	$E_{slab,C2H4}$ (eV)	E_{slab} (eV)	$E_{slab}+E_{C2H4}$ (eV)	$E_{ads,C2H4}$ (eV)	Adsorption Distance (Å)
Pt (111)	-448.17	-413.42	-445.40	-2.76	2.83
Pd (111)	-382.61	-349.23	-381.21	-1.40	2.13
W(110)	-767.75	-733.40	-765.39	-2.37	2.15
Mo(110)	-651.06	-617.05	-649.03	-2.03	2.19
$Ni(111)_{Para}$	-382.77	-349.16	-381.14	-1.63	1.25
$Ni(111)_{Ferro}$	-386.42	-353.03	-385.01	-1.40	1.47
$Fe(110)_{Ferro}$	-494.30	-460.62	-492.60	-1.70	1.61
$Co(001)_{Para}$	-463.62	-430.04	-462.02	-1.60	2.11
$Co(001)_{Ferro}$	-479.59	-446.90	-478.88	-0.70	2.16
$Co_3Mo(001)_{Para}$	-948.18	-913.98	-945.96	-2.22	1.78
$Co_3Mo(001)_{Ferro}$	-949.78	-915.52	-947.50	-2.27	1.82

DOS and Electron Density Maps of Adsorbed Ethylene

During the adsorption of ethylene onto the surface of the metals, ethylene's π orbital overlaps and interacts with the surface metal atoms' empty *d*-orbitals, through which ethylene's π electrons are delocalized to the metal surface and bonding interaction occurs between C and surface metal atoms. Such orbital interaction can be observed by examining the electronic structure and electron density maps of adsorbed ethylene, as pictured in Figure 5.2.

Table 5.2. Carbon-carbon bond length of adsorbed ethylene on metal surfaces.

Surface	C-C bond length (Å)
Pt(111)	1.49
Pd(111)	1.45
W(110)	1.48
Mo(110)	1.48
$Ni(111)_{Para}$	1.45
$Ni(111)_{Ferro}$	1.45
$Fe(110)_{Ferro}$	1.48
$Co(001)_{Para}$	1.46
$Co(001)_{Ferro}$	1.46
$Co_3Mo(001)_{Para}$	1.47
$Co_3Mo(001)_{Ferro}$	1.45

When the partial DOS of the adsorbed ethylene is plotted, such as the one in Figure 5.2, six peaks are featured below E_F. Each peak represents an occupied valence molecular orbital (MO) of ethylene. Electron density maps can be calculated with VASP for each of these peaks,

which were subsequently plotted with VESTA and compared to the images of the MO's of free ethylene calculated by Gaussian (Figure 5.2). This allows for the identification and matching of each DOS peak with its respective MO of the free ethylene molecule.

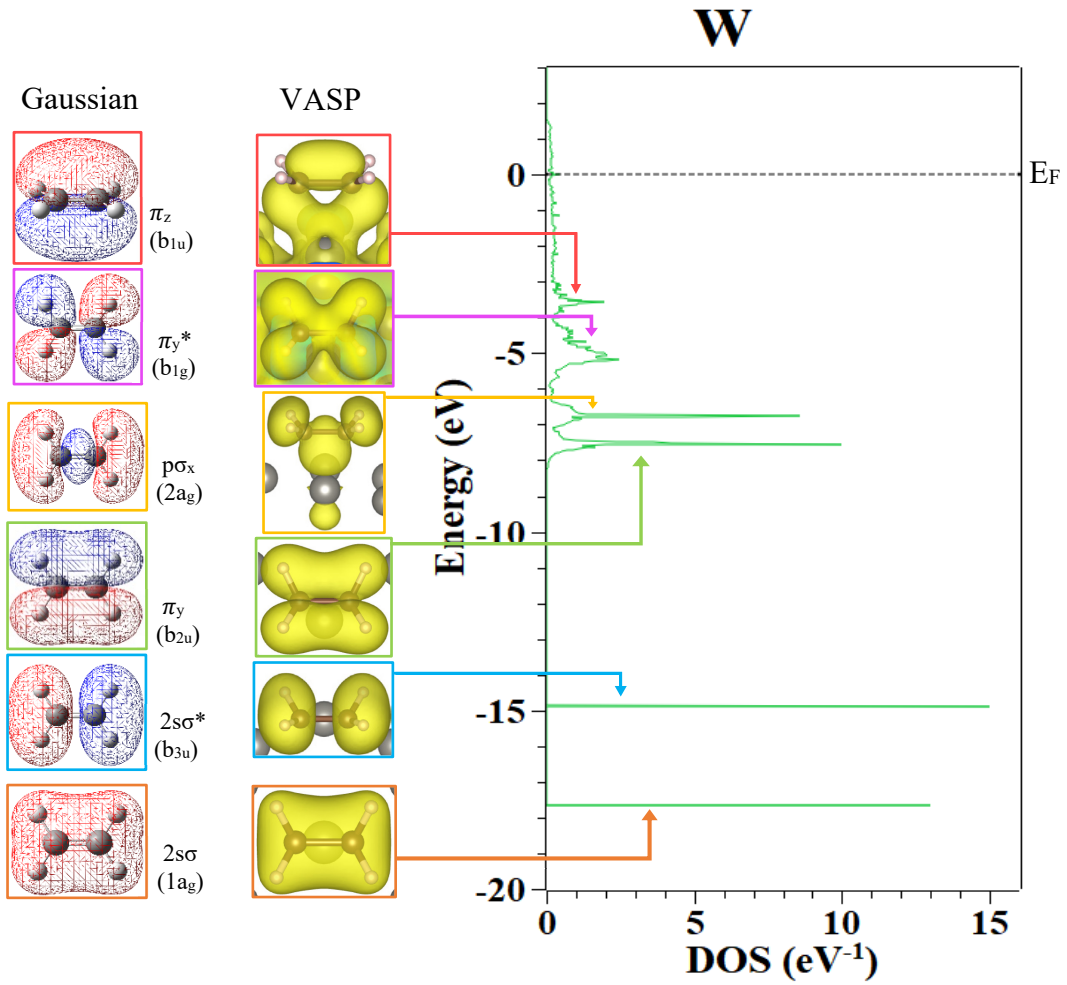

Figure 5.2. The partial DOS of ethylene adsorbed on W(110) surface, the VASP calculated charge density maps for DOS peaks and their comparison with Gaussian[20] calculated free ethylene molecular orbitals.

For free ethylene molecules, the six occupied MOs are at six discrete energy levels. Applying this to ethylene's partial DOS, the six peaks below E_F should be narrow and sharp, like δ functions, at the same discrete energy levels. This can be seen in the next section when non-adsorbed ethylene is discussed (Figure 5.5). When ethylene is adsorbed, its molecular orbitals interact with the surface atoms empty *d*-orbitals, into which ethylene's electrons are delocalized.

This orbital interaction and electron delocalization will cause the six originally discrete peaks to disperse in energy, which is reflected by the broadening of the peaks in ethylene's partial DOS.

Looking at the partial DOS of ethylene on W(110) plane in Figure 5.2, the two lowest peaks representing 2sσ and 2sσ*, are "δ-function-like" sharp peaks, which are like those in the free ethylene molecule. Meaning that these two low-energy MO's have essentially no interaction with the surface W atoms. Comparatively, the higher four peaks, representing π_y, $p\sigma_x$, π_y*, and π_z are much broader. This means the four higher energy MO's do interact with surface W atoms' orbitals to varying degrees. The interaction can be confirmed in the observation of the VASP calculated density maps plotted on VESTA because for these four peaks the electron density of the ethylene evidently merges with the electron density of the W atoms from below.

Among all of the peaks in Figure 5.2, the π_z peak directly below E_F, which represents the highest occupied molecular orbital (HOMO), broadens the most with a small portion even stretching above E_F. The states now above E_F are not occupied anymore. Meaning, that the ethylene's HOMO (π_z) interacts most strongly with the W orbitals since it is partially depopulated. This means the delocalization has occurred due to loss of the HOMO electrons to the surface W atoms.

The partial DOS curves of ethylene adsorbed on the other metals and intermetallics were also calculated and compared in Figure 5.3. From the broadening of the highest peak below E_F, I can see the difference in the interaction between the ethylene's HOMO and the surfaces. For example, on Pt(111) and Pd(111), the ethylene DOS for the topmost peak is completely spread out and is no longer identifiable as a full peak, meaning the adsorbed ethylene's π electrons are largely delocalized. Whereas, looking at the DOS of ethylene on W(110) the peak is much more

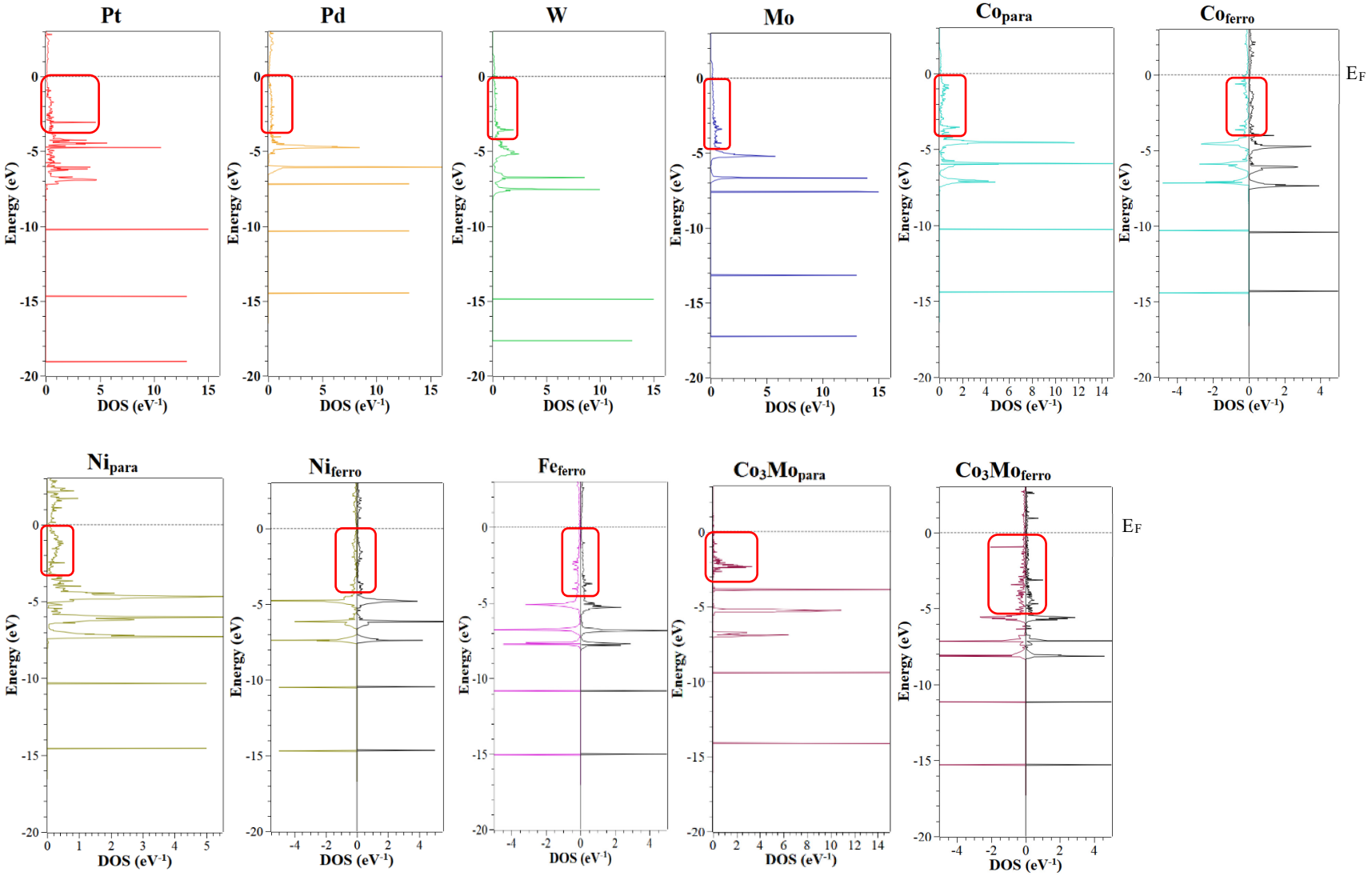

Figure 5.3. Partial DOS of ethylene adsorbed on the surfaces of metals and intermetallics. The red box indicates where the broadened π_z peak is located, which are too broad to be discernable.

definable, meaning ethylene's π electrons were less delocalized. This shows that ethylene's HOMO(π_z) has more effective interactions with Pt's and Pd's empty surface atomic orbitals than with those of the other metals, such as W, based on a visual evaluation. Since Pt and Pd are the most common catalysts in olefin hydrogenation, such effective ethylene-surface orbital interactions must be another characteristic of an efficient catalyst and a key factor for the effective adsorption of ethylene on the surface and the subsequent hydrogenation reaction.

With the ferromagnetic compounds, in Figure 5.3, ethylene's partial DOS are plotted separately for the two spins. The same peaks representing ethylene's MO's can still be visually evaluated the same way. For the most part, the DOS curves are symmetrical between the two spins, especially for the low-energy peaks. This is consistent with the fact that a free ground state ethylene molecule is diamagnetic. So, in each MO, the spin-up and spin-down electrons are always paired up at the same energy level. The peak representing the π_z MO spreads out and is not discernible for the for the partial DOS of ethylene adsorbed on these ferromagnetic metals or intermetallics. However, in each case no significant difference is observed between the two spins. This is in contrast with the bulk and slab total DOS in Figure 3.1 because they exhibit significant asymmetry between the two spins.

The asymmetry results in the majority spin having an insignificant number of empty *d*-states around E_F and only the minority spin having abundant empty *d*-states to accommodate the π electrons delocalized from ethylene. This indicates that, to accommodate the diamagnetic electrons with both spins from ethylene, the metals "flip" some of the electrons from majority spin to minority spin to provide empty states. This partially explains why, in Table 5.1, $E_{ads,C2H4}$ is much lower for the ferromagnetic vs. the paramagnetic calculations of each ferromagnetic metal since the rearrangement metal of electrons would cost a certain amount of energy. This

flipping of spins also contributes to the energy penalty for ethylene adsorption. Therefore, ferromagnetism is an undesirable feature for heterogeneous hydrogenation catalyst.

The numerical results in Table 5.1 still show that the hypothetical non-spin-polarized calculations for the ferromagnetic metals and intermetallics result in more negative $E_{ads,C2H4}$ but must still be considered unrealistic. For each ferromagnetic metal, adsorption still occurs but $E_{ads,C2H4}$ is much less negative than Pt with the average adsorption energy being around half of Pt's. The most favorable of ferromagnetic metals and intermetallics is Co_3Mo. For Co_3Mo it is apparent that the ferromagnetic calculations yielded the best result both visually in Figure 5.3 but also in Table 5.1. Additionally, Co_3Mo yielded better results than both Co and Mo separately. This would suggest that these two metals work better together than separately for the adsorption of ethylene.

Ethylene Progressively Approaching Surfaces

While VASP's structural optimization simulates the adsorption result, the adsorption process, especially how the π_z MO interacts with the metal or intermetallic surface atomic orbitals while ethylene is approaching the surface, is still not clear. In order to analyze this, a series of static calculations, meaning no structural optimization occurs, were performed at different ethylene-surface distances. The partial DOS of ethylene was calculated initially at a distance so far from the surface, between 6.2-7.4 Å, that no bonding can occur between ethylene and the metal surface atoms. Then the distance between ethylene and the surface was progressively decreased until it reached the adsorption distance, which was the ethylene-surfaces distance when ethylene is completely adsorbed. The progressive lowering of ethylene can be

seen in Figure 5.4 on the surface of Pt. This systematic lowering was done for all metals and intermetallic compounds previously used and the partial DOS of ethylene was calculated.

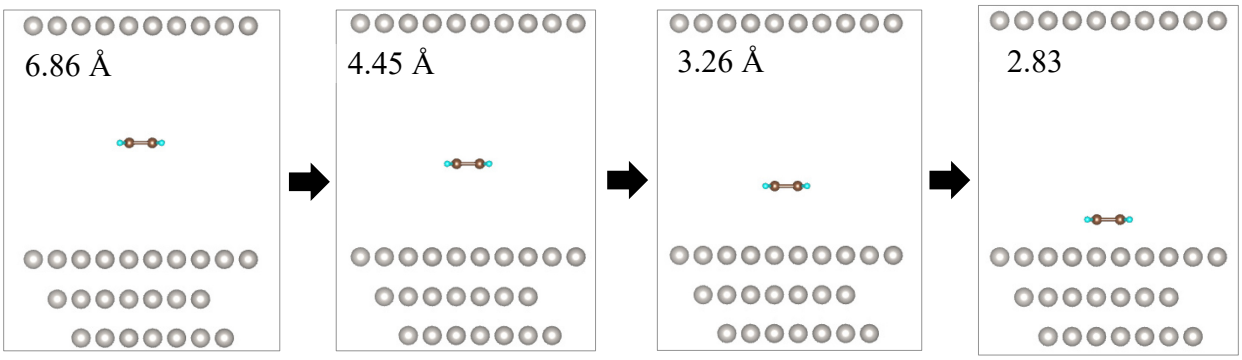

Figure 5.4. Progressive lowering of ethylene towards the surface of Pt.

Figure 5.5 shows the partial DOS of ethylene progressively approaching the Pt(111), W(110), and Fe(110) surfaces. For all three cases, initially, when ethylene and its π_z MO is too far from the surfaces to interact, each metal's π_z DOS peak is sharp and thin. As ethylene begins to lower the peak visibly broadens and the peak spreads out over a broader energy range. This suggests that the π_z orbital starts to interact with the surface atoms' orbitals and the π_z electrons have become delocalized into the metal atomic orbitals. The change is most noticeable with ethylene on Pt when the ethylene is 2.83 Å from the surface of the slab, in which the π_z DOS peak is not discernible, just like when the ethylene fully adsorbed on Pt(11) during the optimization shown in Figure 5.3.

Meanwhile, the π_z peak broadened until it was indiscernible for the approach of ethylene on the W and Fe surfaces (Figure 5.5) as well as other metals. Figure 5.6 shows the final-step partial DOS, when the π_z peak is indiscernible and at the adsorption distance, of ethylene on the other metal surfaces including Pd, Mo, Ni, Co, and Co_3Mo. The full approach of all final surfaces shown in Figure 5.5 can be found in Appendix B. If the disappearance of the π_z peak

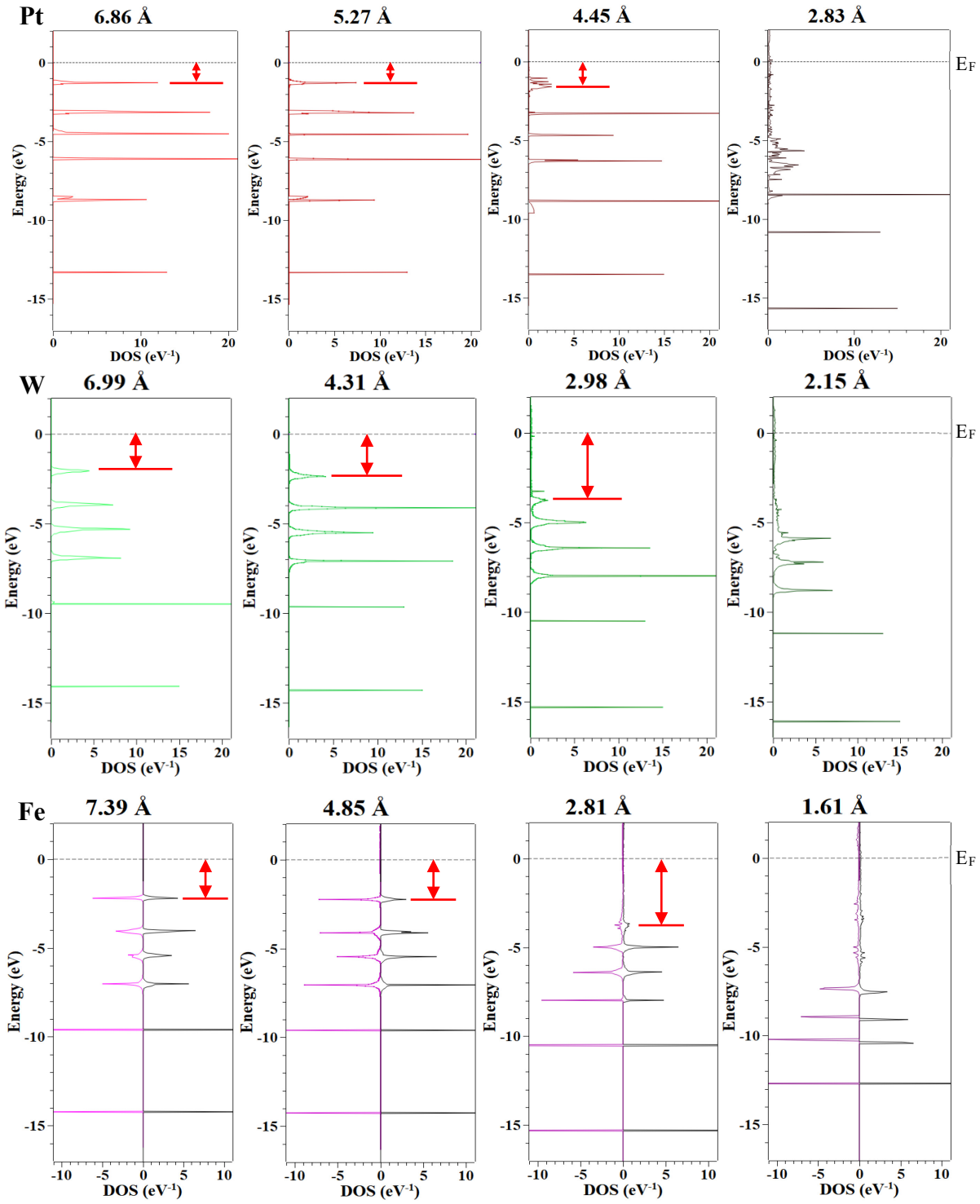

Figure 5.5. Progressive lowering of ethylene on Pt, W, and Fe. Where the arrows indicate the distance between the π_z peak and E_F to highlight the change in energy as ethylene's distance from the surface decreases.

due to broadening is the indicator of bond formation between ethylene and the surface atoms, it can be seen from Figures 5.5 and 5.6 that ethylene bonds with different metal surfaces at different distances. Which leads to the conclusion that each surface does have the ability to bond with ethylene but to varying degrees. For example, Pt finishes bonding at 2.83 Å, which is a much farther distance than every other surface.

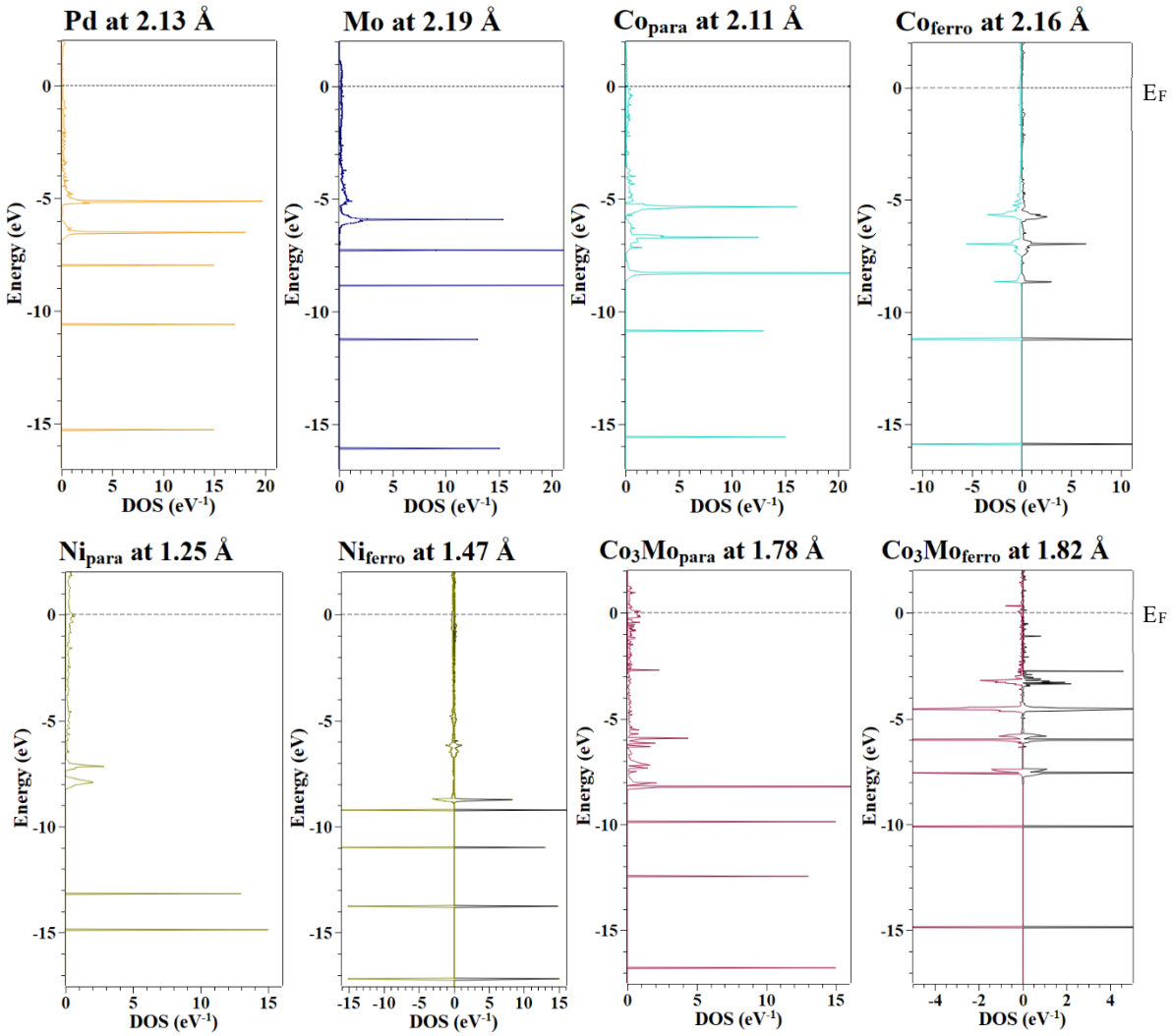

Figure 5.6. Final DOS of lowered ethylene on Pd, Mo, Co, Ni, and Co_3Mo. The π_z peaks are too broad to be discernable like those seen in Figure 5.3.

To quantitatively evaluate the broadening of each discernible π_z peak, I zoomed in and digitized a series of DOS points (D_i) versus Energy (E_i) data. I then located the central energy level (E_c) of the π_z peak which divided the peak area into two equal halves. This E_c is the weighted mean value of all E_i's with D_i's being the weights. Then we calculated the standard deviation using Equation 5.1, which quantifies the deviation of all E_i's from E_c and thus the peak width. The larger the standard deviation is, the broader the peak is and the more significant the ethylene-surface interaction becomes. This "standard deviation" can be calculated for all π_z peaks before they spread so much that they become indistinguishable once ethylene gets very close to the surfaces. The results of Equation 5.1 can be seen in Figure 5.7 showing the broadening of the π_z peaks as the ethylene -surface distance decreased.

$$stdv = \sqrt{\frac{\sum D_i \times (E_i - E_c)^2}{\sum D_i}} \qquad \text{Equation 5.1}$$

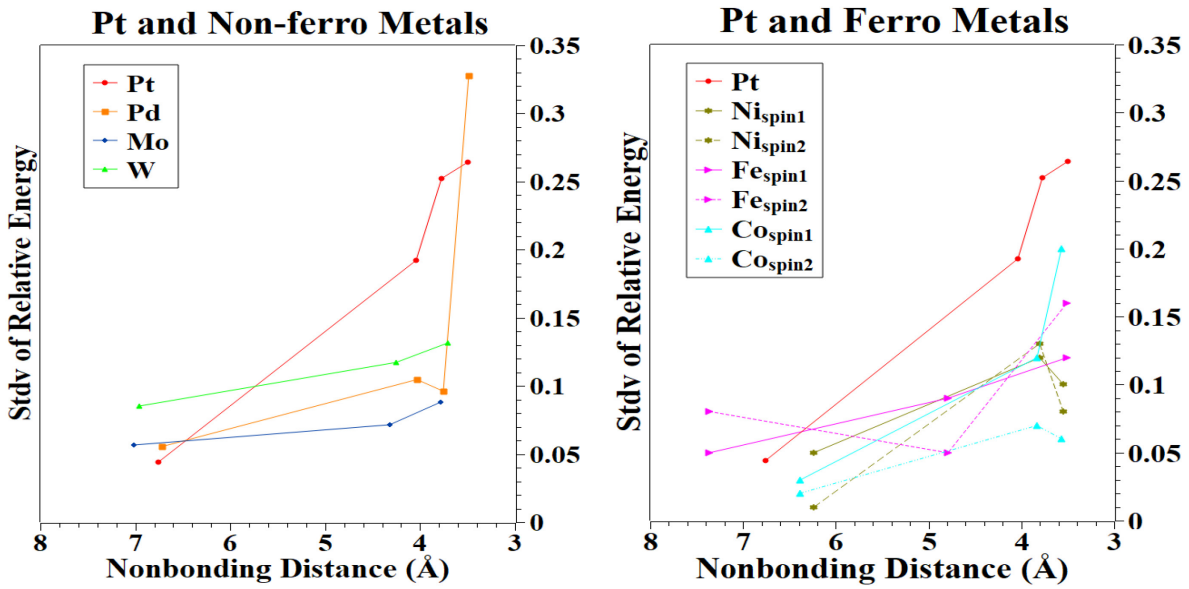

Figure 5.7. The standard deviation of the ethylene π_z peak at varying distances above each metal surface.

In general, with the progressive approaching of ethylene to the surfaces, the standard deviation increases but at different rates for each metal, which is consistent with the visual observation of peak broadening in Figure 5.5. Out of all the metals, ethylene above Pt shows the earliest π_z peak broadening. The standard deviation reaches ~0.25 when ethylene is over 4 Å away from the Pt surface. A standard deviation of ~0.2 is also reached with Pd and Co_{spin1} surfaces but at a much shorter ethylene-surface distance at around 3.6 Å. At the same distance as ethylene on Pt, the other metal surfaces' standard deviations have not reached a similar level as seen in Figure 5.5. This means that ethylene's π_z MO already substantially interacts with Pt surface orbitals from a far distance while not interacting significantly with the other metals until they are much closer to their surfaces.

For the ferromagnetic metals, the two spins were evaluated separately and are both plotted. At any certain ethylene surfaces distance, the two spins always broaden differently, this is especially true for Co. This means that ethylene's π_z electrons in opposite spins are delocalized in differing degrees on each of these ferromagnetic metal surfaces.

From the three sets of partial DOS in Figure 5.5, it can also be seen that as ethylene progressively approaches the surfaces all DOS peaks' energy lower with respect to E_F. This can be attributed to the lowering in potential energy of ethylene's electrons as they approach the surface metal atoms and experience attraction from the metal nuclei. This energy lowering, especially of the π_z peak, is unfavorable for ethylene's adsorption. As stated before in Chapter 4, the metals' states or orbitals available to accommodate the delocalized electrons from the adsorbates are the low-energy empty *d*-states (LUMO) immediately above the E_F. The larger the π_z to E_F energy difference, the more difficult it becomes for bonding to occur between the ethylene and the metal surfaces because this π_z to E_F gap represents the energy penalty that

ethylene's π_z electrons must pay in order to delocalize into the empty *d*-states above E_F. So, the metals which afford a smaller π_z to E_F penalty will start bonding with ethylene sooner as ethylene approaches the surface.

Because the E_F is always the reference energy at 0 eV in a DOS figure, the energy centers for the π_z peaks (E_c in Equation 5.1) can be used to quantify the π_z to E_F gaps. A less negative E_c means a smaller π_z to E_F energy difference. The π_z peak E_c of ethylene above the metal surfaces are compared in Figure 5.8.

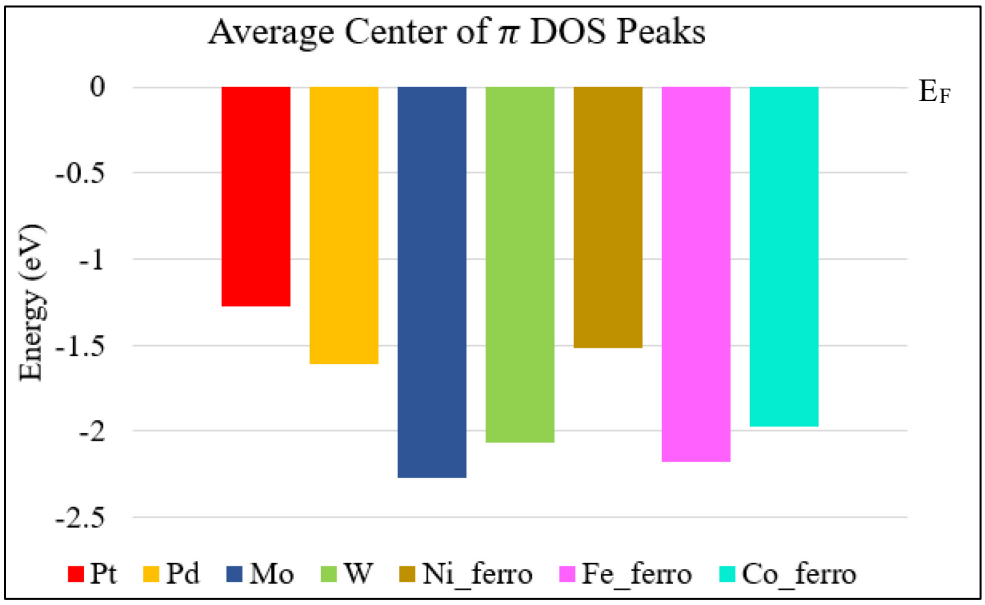

Figure 5.8. Energy distance of the center of each π-peak from E_F.

The E_c was obtained when ethylene was at the farthest distance from each surface, between 6.2-7.4 Å. They give a good understanding of the π_z to E_F energy difference before bonding occurs between ethylene and the surfaces. The less negative the E_c is the smaller the π_z to E_F energy difference is and the easier it is for ethylene to bond with that given metal. In figure 5.8 it is apparent that with Pt ethylene's E_c is the least negative at -1.27 eV, with the next closest being Ni around -1.5 eV and Pd around -1.6 eV. Besides these two, all the other surfaces have

much more negative E_c's than Pt. This can explain why, when progressively approaching, ethylene begins interacting with the Pt surface the earliest – π_z to E_F energy difference is the smallest. For the other metals, due to their larger π_z to E_F energy difference significant bonding occurs much later during ethylene's approach.

CONCLUSION

After comparing Pt to the other metals and intermetallic compounds with computation, there is a better understanding of why Pt is the most effective catalyst for the hydrogenation of olefins. By comparing the DOS of bulk metals and metal slabs without adsorbates and the H_2 and ethylene adsorption, Pt was the most ideal and effective in each case which is consistent with the experimental findings in Table 1.2. Table 6.1 summarizes the most important findings in the previous chapters.

For the bulk metals and metal slabs, Pt had abundant empty *d*-states right at and directly above the E_F. This is a desirable feature because these low-energy empty states are the ones accommodating electrons from the adsorbate molecules and directly participate in bonding between the metal surface and adsorbates. Besides Pt, abundant states at E_F were also observed for Pd and Fe_7Mo_6. Pd is also frequently used as a hydrogenation catalyst, but Fe_7Mo_6 did not exhibit any catalysis in the hydrogenation of 1-octene. For the ferromagnetic species, Fe, Co, Ni, and Co_3Mo, the hypothetical paramagnetic calculations resulted in abundant states at and directly above E_F, but the real ferromagnetic calculations display only moderately abundant states around E_F. This indicates that ferromagnetism greatly decreases the abundancy in low-energy *d*-states and thus compromises catalytic efficiency. So, abundant low-energy empty *d*-states alone does not necessarily render an effective catalyst.

From adsorption energies, $E_{ads,H2}$ are all negative, except for Co_3Mo, showing that all of the metals are able to adsorb H_2 and break the H-H bond but to varying thermodynamic stability. Pt performed the best of all the surfaces tested with the most negative adsorption energy. This means the Pt produced the most thermodynamically stable adsorption of H_2.

Table 6.1. Summary of results.

	Empty *d*-States at E_F*	E_{adsH2}	$E_{adsC2H4}$	π_z-Peak Center	C_2H_4 Adsorption Distance (Å)
Pt (111)	Abundant	-1.77	-2.76	-1.27	2.83
Pd (111)	Abundant	-0.84	-1.40	-1.61	2.25
W(110)	Not abundant	-1.32	-2.37	-2.06	2.25
Mo(110)	Not abundant	-1.38	-2.03	-2.27	2.19
$Ni(111)_{Para}$	Abundant	-1.97	-1.63	-	1.25
$Ni(111)_{Ferro}$	Abundant for minority spin	-1.64	-1.40	-1.52	1.47
$Fe(110)_{Ferro}$	Moderately abundant for majority spin	-1.65	-1.70	-2.18	1.61
$Co(001)_{Para}$	Abundant	-1.37	-1.60	-	2.11
$Co(001)_{Ferro}$	Moderately abundant for minority spin	-1.19	-0.70	-1.97	2.11
Co_3Mo_{Para}	Abundant	-1.14	-2.22	-	1.78
Co_3Mo_{Ferro}	Moderately abundant for minority spin	1.00	-2.27	-	1.82
Fe_7Mo_6	Abundant	-1.77	-	-	-

*Abundance is based upon the DOS at E_F in Figure 3.1.

With ethylene, $E_{ads,C2H4}$ are also negative, meaning all the metals were again able to adsorb ethylene with varying stability. Again, Pt(111) affords the most stable adsorption. Each surface caused the lengthening of the C─C bond which indicated the partial breaking of the C═C double bond due to the delocalization of the ethylene's electrons in HOMO (π_z) to the metal atoms' orbitals. Between $E_{ads,H2}$ and $E_{ads,C2H4}$, $E_{ads,C2H4}$ shows larger variation among the metals

and intermetallics, suggesting that, instead of H_2, it is the ability of the metal to adsorb C_2H_4 that affects the catalytic performance the most.

The adsorption of H_2 and alkene molecules are the initial steps in catalyzed hydrogenation. In this process, a more negative adsorption energy means the adsorption and desorption equilibria are shifted more towards the adsorption, which means higher surface coverage of the catalyst's surface by both H_2 and alkene molecules and a higher reaction rate on the surface. Even though desirable, negative adsorption energy alone does not necessarily indicate an efficient catalyst just like the abundancy of *d*-states at E_F. For instance, W and Mo both have $E_{ads,H2}$ and $E_{ads,C2H4}$ more negative than the ferromagnetic metals and intermetallics. However, when used as a catalyst in the hydrogenation of 1-octene, W and Mo exhibit no activity. This is because a very negative E_{ads} means a very firm adsorption, which, if too firmly adsorbed, may limit the surface diffusion of adsorbate molecules, which is an essential step in surface reactions following adsorption. For the comparison of the hypothetical paramagnetic and real ferromagnetic calculations for Ni, Co, and Co_3Mo demonstrate that ferromagnetism leads to less negative adsorption energies. The ferromagnetism thus compromises the adsorption and as a result the catalysis.

When observing the progressive lowering of ethylene molecules on the surface of the metals and intermetallics, informational results on the activity between the adsorbate and the surface are provided. With ethylene's approach, its π_z starts to interact with the surface metal atoms' orbitals and is manifested in the broadening of the π_z peak in ethylene's partial DOS. This can be viewed as the beginning of bond formation between ethylene and the surfaces. The onset of this interaction occurs at different ethylene-surface distances for each metal. For Pt, the π_z peak begins to broaden around 4.5 Å from the surface. Once it begins to broaden it does so

quickly as the distance is shortened. On the other hand, the other metals and intermetallics π_z peaks do not broaden as significantly until ethylene is substantially closer to their surfaces. This difference can be attributed to the relative energy difference between the π_z peak and the empty *d*-states, which is quantified by the π_z peak center. This energy difference defines the energy penalty for ethylene's π_z electrons to delocalize into the empty *d*-states of the metal. Pt features the least negative π_z peak center and thus the lowest energy penalty in the ethylene-surface electron transfer and bond formation. In the end, ethylene's adsorption onto the Pt surfaces is completed when it is still 2.83 Å from the surface while the other surfaces require ethylene to be much closer to be fully adsorbed.

Overall, the fact that Pt is most effective in each of these instances bolsters the reason Pt is still being used as a hydrogenation catalyst despite the extra cost associated with it. The investigation of a binary intermetallic compound to replace Pt as a catalyst is clearly not straightforward. The idea of "like electronic structure, like catalysis" is complicated and the electronic structures have to be investigated from multiple angles such as the ones detailed in this thesis. From these investigations, our understanding of the electronic structure for these metals as well as the adsorption of H_2 and alkenes have been expanded. To fill out this knowledge in future work, other crystallographic planes as well as surfaces defects like holes, adatoms, and steps should be studied. Simulation of adsorption and diffusion of the larger adsorbed alkene molecules as well as the desorption of the hydrogenation products or alkanes should also be investigated. With Pt's catalytic characteristics more clearly defined, more rigorous examination, tailoring, and design of additional binary intermetallic compounds can be achieved, in the hope of obtaining efficient base metal hydrogenation catalysts.

REFERENCES

(1) Speight, J. G. Handbook of Petroleum Refining; Chemical industries; *CRC Press, Taylor & Francis Group*, Boca Raton, **2017**.

(2) Tsai, A. P.; Kameoka, S.; Nozawa, K.; Shimoda, M.; Ishii, Y. Intermetallic: A Pseudoelement for Catalysis. *Acc. Chem. Res.* **2017**, *50* (12), 2879–2885. https://doi.org/10.1021/acs.accounts.7b00476.

(3) Hobson, P. Platinum Set for Third Year of Deficit as Industry Demand Surges, WPIC Says. *Reuters*. May 17, 2021. https://www.reuters.com/business/environment/platinum-set-third-year-deficit-industry-demand-surges-wpic-says-2021-05-17/ (accessed 2022-11-18).

(4) Current Tungsten / Tungsten Price , Historical Prices, USA, China, Europe, Asia, Australia Prices. *ScrapMonster*. https://www.scrapmonster.com/metal-prices/minor-metals/tungsten-tungsten/815 (accessed 2023-06-23).

(5) Daily Metal Price: Iron Ore Price (USD / Kilogram) for the Last Month. https://www.dailymetalprice.com/metalprices.php?c=fe&u=kg&d=1 (accessed 2022-11-09).

(6) Wang, F. Unpublished Work. Missouri State University, Springfield Missouri, **2023**.

(7) Kresse, G.; Marsman, M.; Poeltl, M.; Kaltak, M.; Hirsh, C.; Karsai, F.; Schlipf, M.; Miranda, H.; Werner, C.; Emin, A.; Singraber, A.; Huebsch, M.-T.; Wolloch, M.; Tal, A.; Tran, F.; Lahnsteiner, J.; Melo, P. VASP - Vienna Ab initio Simulation Package. https://www.vasp.at/ (accessed 2022-11-17).

(8) Category:Theory - Vaspwiki. https://www.vasp.at/wiki/index.php/Category:Theory (accessed 2023-06-24).

(9) Nondestructive Evaluation Physics : Magnetism. https://www.nde-ed.org/Physics/Magnetism/MagneticMatls.xhtml (accessed 2023-06-27).

(10) Momma, K.; Izumi, F. VESTA 3 for Three-Dimensional Visualization of Crystal, Volumetric and Morphology Data. *J Appl Cryst* **2011**, *44* (6), 1272–1276. https://doi.org/10.1107/S0021889811038970.

(11) Grimme, S.; Antony, J.; Ehrlich, S.; Krieg, H. A Consistent and Accurate Ab Initio Parametrization of Density Functional Dispersion Correction (DFT-D) for the 94 Elements H-Pu. *J. Chem. Phys.* **2010**, *132* (15), 154104. https://doi.org/10.1063/1.3382344.

(12) ISMEAR - Vaspwiki. https://www.vasp.at/wiki/index.php/ISMEAR (accessed 2023-04-08).

(13) Press, W. H. Numerical Recipes : The Art of Scientific Computing; *Cambridge University Press*, New York, **1986**.

(14) Ungerer, M. J.; Santos-Carballal, D.; Cadi-Essadek, A.; van Sittert, C. G. C. E.; de Leeuw, N. H. Interaction of H2O with the Platinum Pt (001), (011), and (111) Surfaces: A Density Functional Theory Study with Long-Range Dispersion Corrections. *J. Phys. Chem. C* **2019**, *123* (45), 27465–27476. https://doi.org/10.1021/acs.jpcc.9b06136.

(15) Skriver, H. L.; Rosengaard, N. M. Surface Energy and Work Function of Elemental Metals. *Phys. Rev. B* **1992**, *46* (11), 7157–7168. https://doi.org/10.1103/PhysRevB.46.7157.

(16) Huber, K. P.; Herzberg, G. Constants of Diatomic Molecules. In *Molecular Spectra and Molecular Structure: IV. Constants of Diatomic Molecules*; Huber, K. P., Herzberg, G., Eds.; Springer US: Boston, MA, **1979**; pp 8–689. https://doi.org/10.1007/978-1-4757-0961-2_2.

(17) Schwarzer, M.; Hertl, N.; Nitz, F.; Borodin, D.; Fingerhut, J.; Kitsopoulos, T. N.; Wodtke, A. M. Adsorption and Absorption Energies of Hydrogen with Palladium. *J. Phys. Chem. C* **2022**, *126* (34), 14500–14508. https://doi.org/10.1021/acs.jpcc.2c04567.

(18) Ethylene. *Wikipedia*; **2022**.

(19) Ethane. *Wikipedia*; **2023**.

(20) Frisch, M.; Trucks, G.; Schlegel, H.; Scuseria, G.; Robb, M.; Cheeseman, J.; Scalmani, G.; Barone, V.; Mennucci, B.; Petersson, G.; Nakatsuji, H.; Caricato, M.; Li, X.; Hartchian, H.; Izmaylov, A.; Bloino, J.; Zheng, G.; Sonnenberg, J.; Hada, M.; Ehara, M.; Toyota, K.; Fukuda, R.; Hasegawa, J.; Ishida, M.; Nakajima, T.; Honda, Y.; Kitao, O.; Nakai, H.; Vreven, T.; Montgomery, J.; Peralta, J.; Ogliaro, F.; Bearpark, M.; Heyd, J.; Brothers, E.; Kudin, K.; Staroverov, V.; Kobayashi, R.; Normand, J.; Raghavachari, K.; Rendell, A.; Burant, J.; Iyengar, S.; Tomasi, J.; Cossi, M.; Rega, N.; Millam, J.; Klene, M.; Knox, J.; Cross, J.; Bakken, V.; Adamo, C.; Jaramillo, J.; Gomperts, R.; Stratmann, R.; Yazyev, O.; Austin, A.; Cammi, R.; Pomelli, C.; Ochterski, J.; Martin, R.; Morokuma, K.; Zakrzewski, V.; Voth, G.; Salvador, P.; Dannenberg, J.; Dapprich, S.; Daniels, A.; Farkas, Ö.; Foresman, J.; Ortiz, J.; Cioslowski, J.; Fox, *Gaussian 09.* D. Gaussian Inc., Wallingford CT, **2009**.

APPENDICES

Appendix A: Additional Bulk, Slabs, and Hydrogen Adsorption

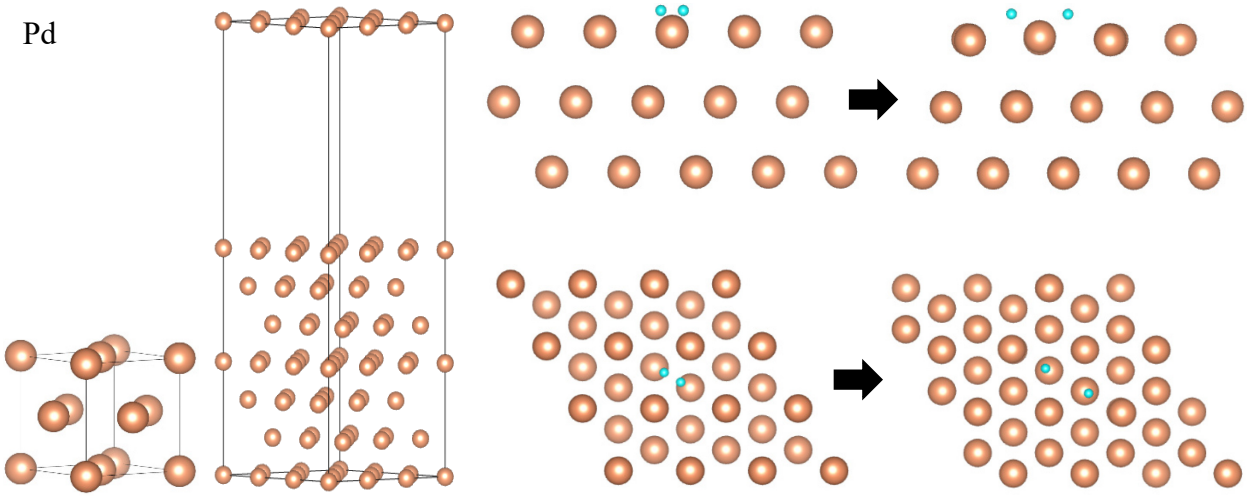

Appendix A-1. Pd unit cell for bulk, slab, unadsorbed H_2, and adsorbed H_2.

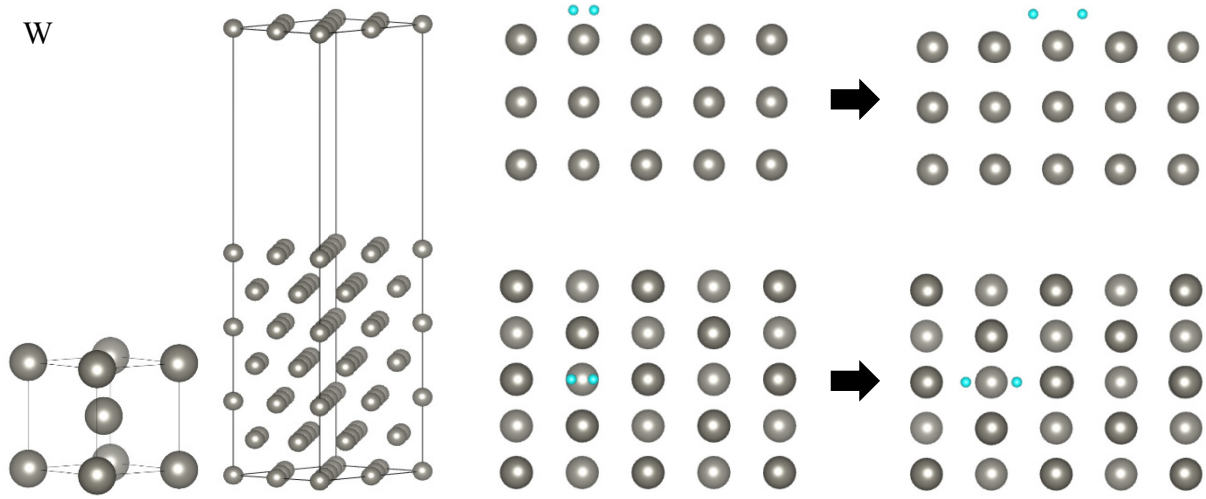

Appendix A-2. W unit cell for bulk, slab, unadsorbed H_2, and adsorbed H_2.

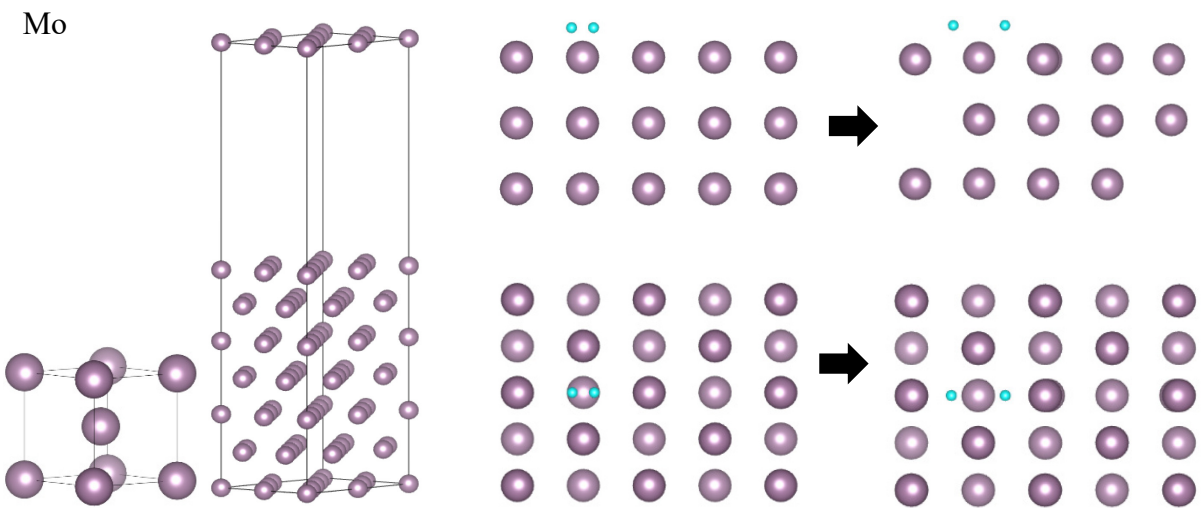

Appendix A-3. Mo unit cell for bulk, slab, unadsorbed H_2, and adsorbed H_2.

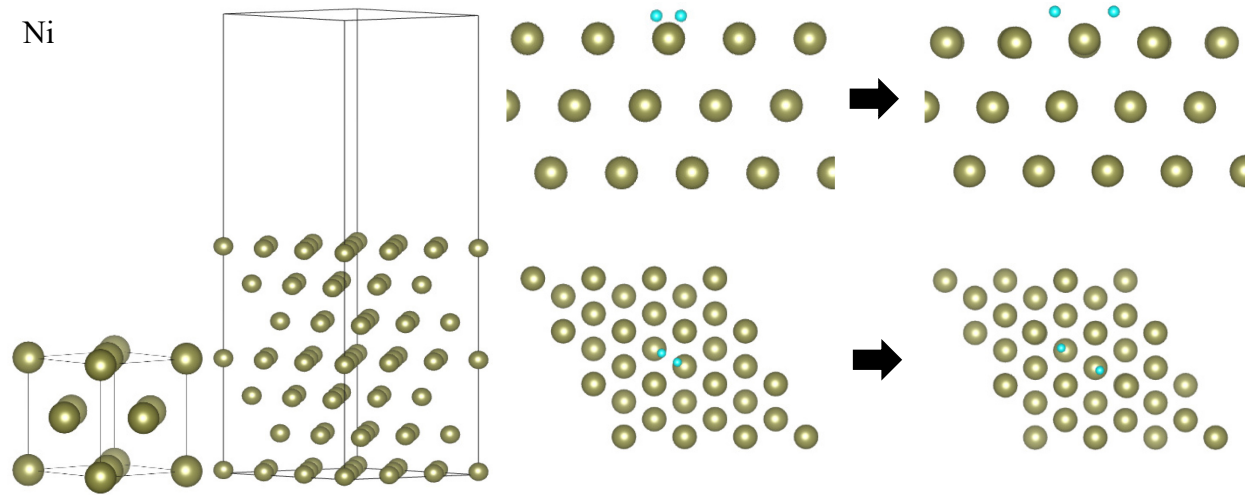

Appendix A-4. Ni unit cell for bulk, slab, unadsorbed H_2, and adsorbed H_2.

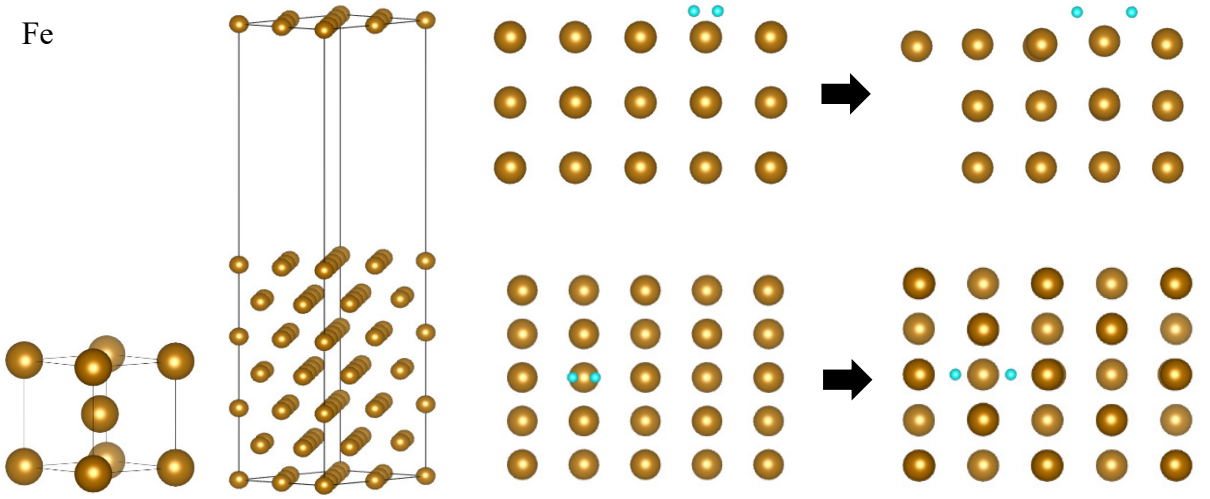

Appendix A-5. Fe unit cell for bulk, slab, unadsorbed H_2, and adsorbed H_2.

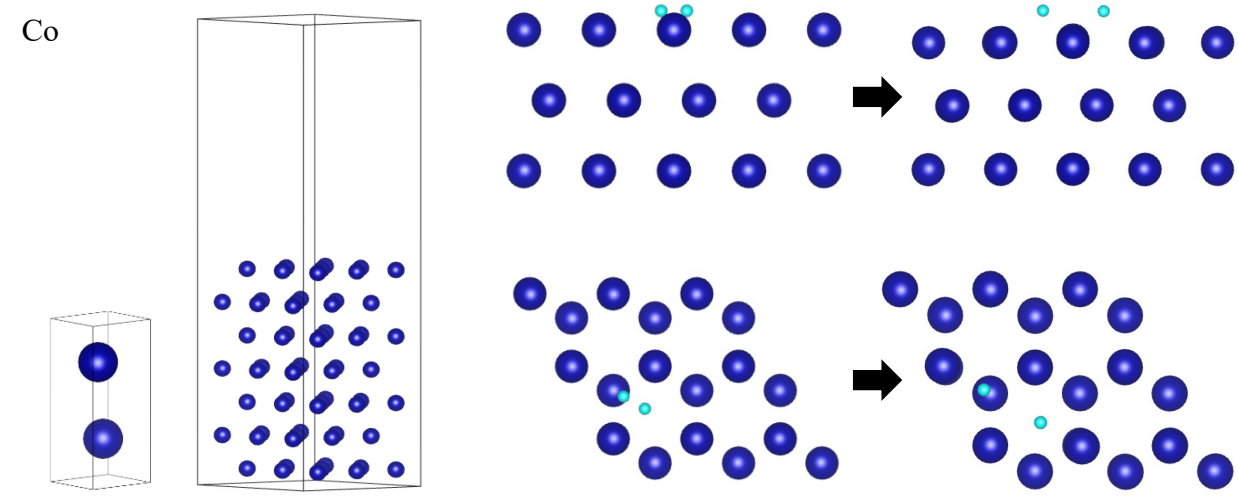

Appendix A-6. Co unit cell for bulk, slab, unadsorbed H_2, and adsorbed H_2.

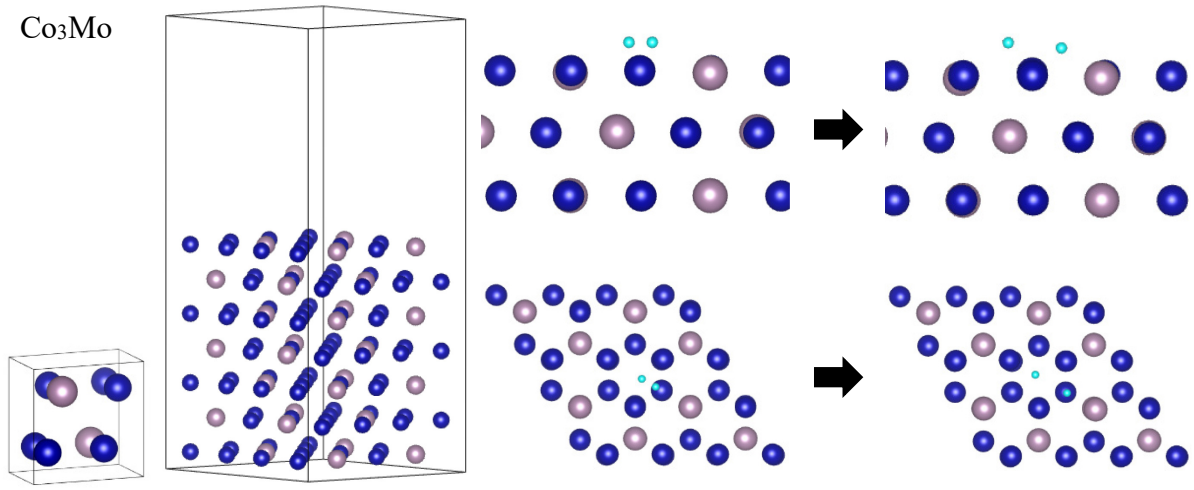

Appendix A-7. Co_3Mo unit cell for bulk, slab, unadsorbed H_2, and adsorbed H_2.

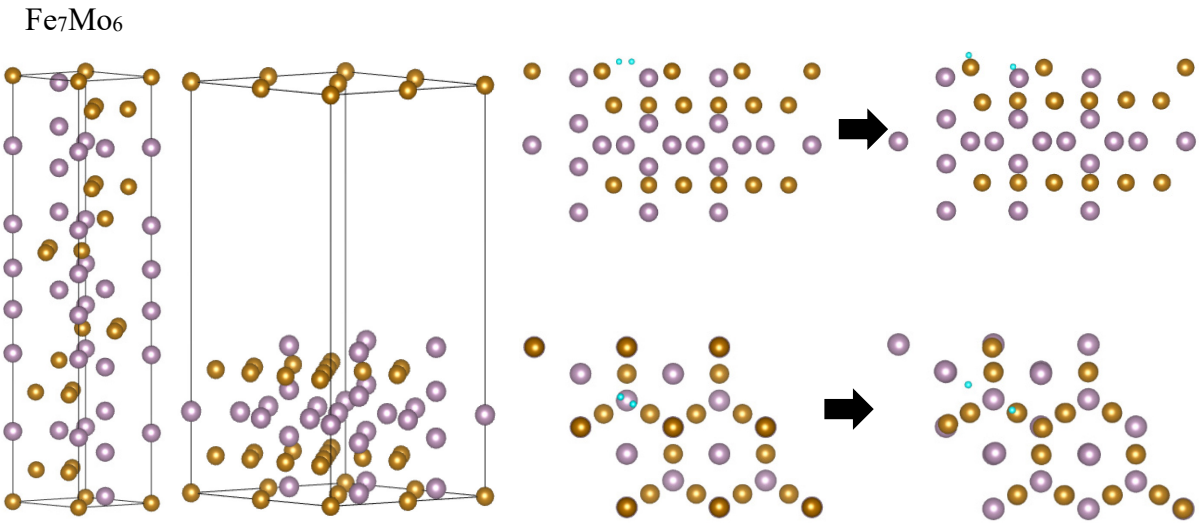

Appendix A-8. Fe_7Mo_6 unit cell for bulk, slab, unadsorbed H_2, and adsorbed H_2.

Appendix B: Additional Partial DOS of Ethylene Progressively Approaching Surfaces

Pd

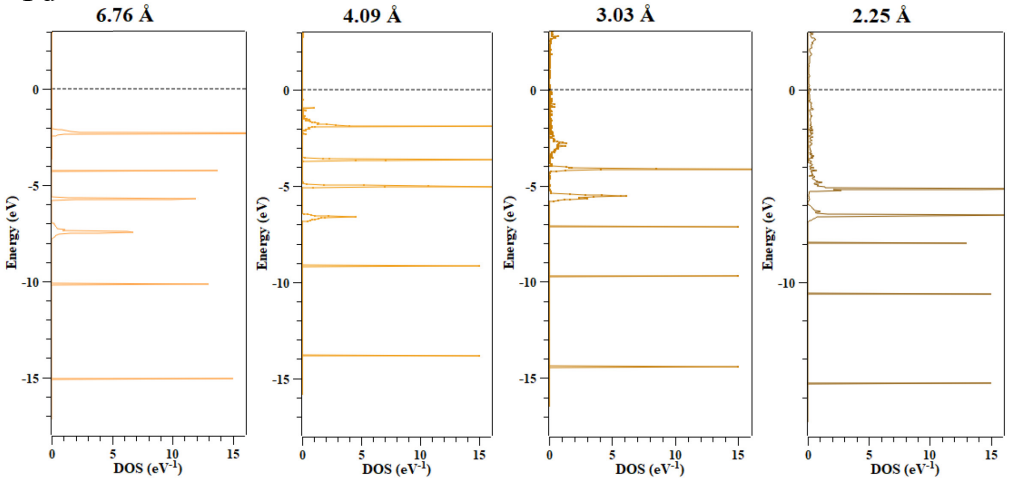

Appendix B-1. Partial DOS of ethylene progressively approaching the surface of Pd.

Mo

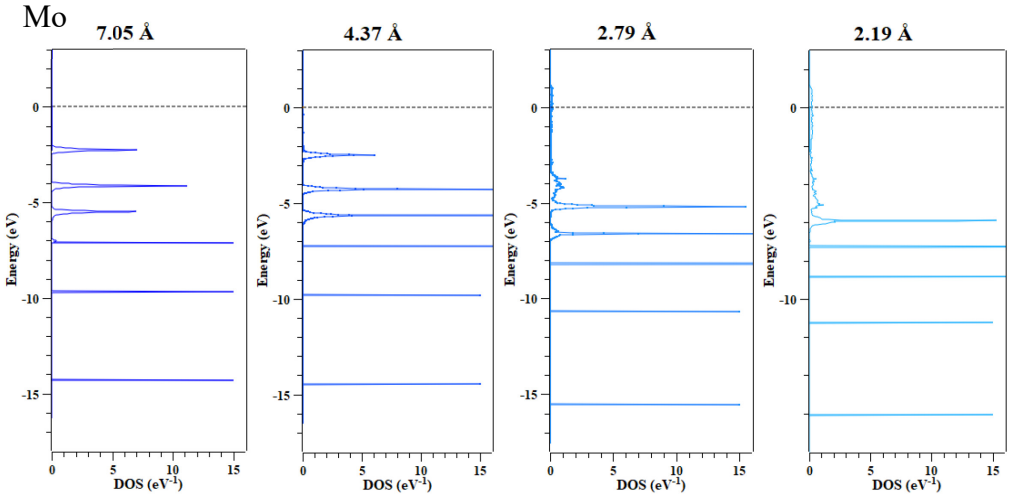

Appendix B-2. Partial DOS of ethylene progressively approaching the surface of Mo.

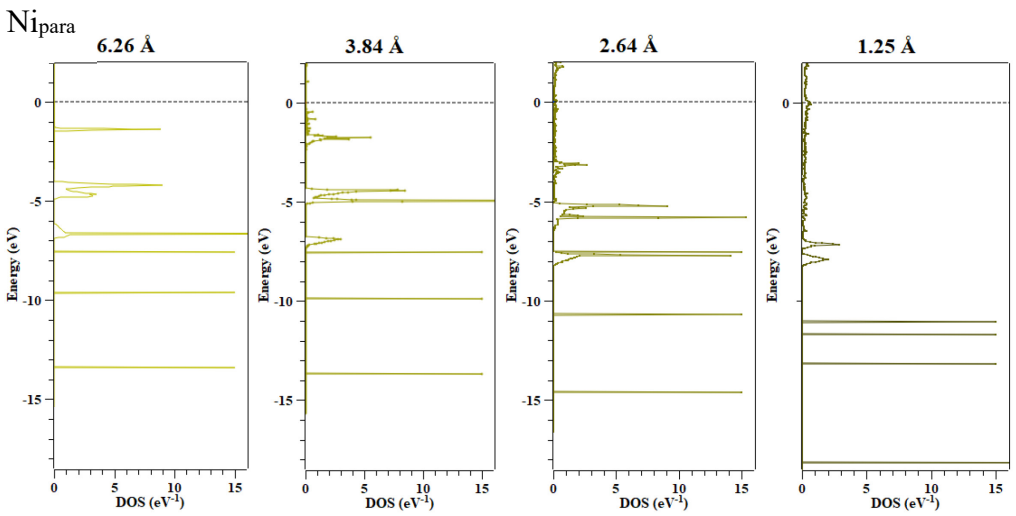

Appendix B-3. Partial DOS of ethylene progressively approaching the surface of Ni_{para}.

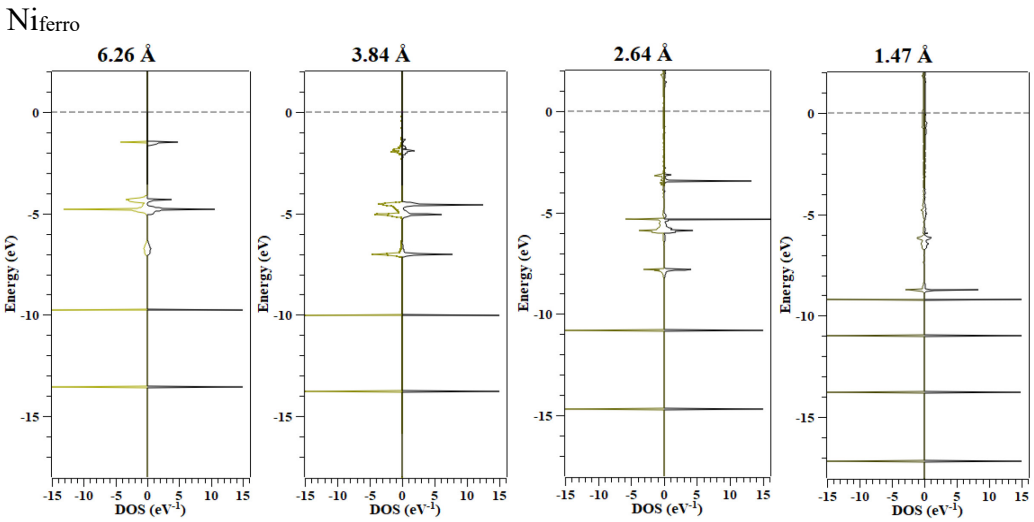

Appendix B-4. Partial DOS of ethylene progressively approaching the surface of Ni_{ferro}.

Co_{para}

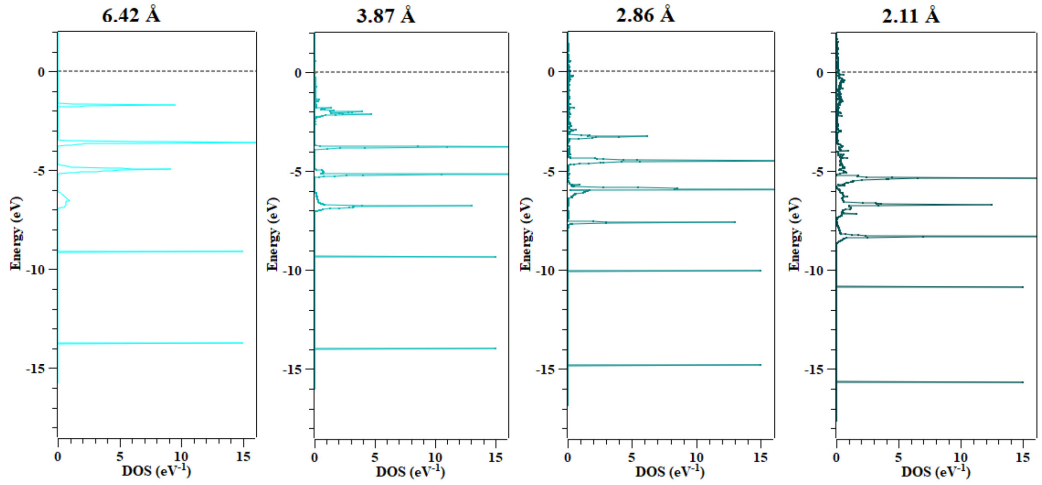

Appendix B-5. Partial DOS of ethylene progressively approaching the surface of Co_{para}.

Co_{ferro}

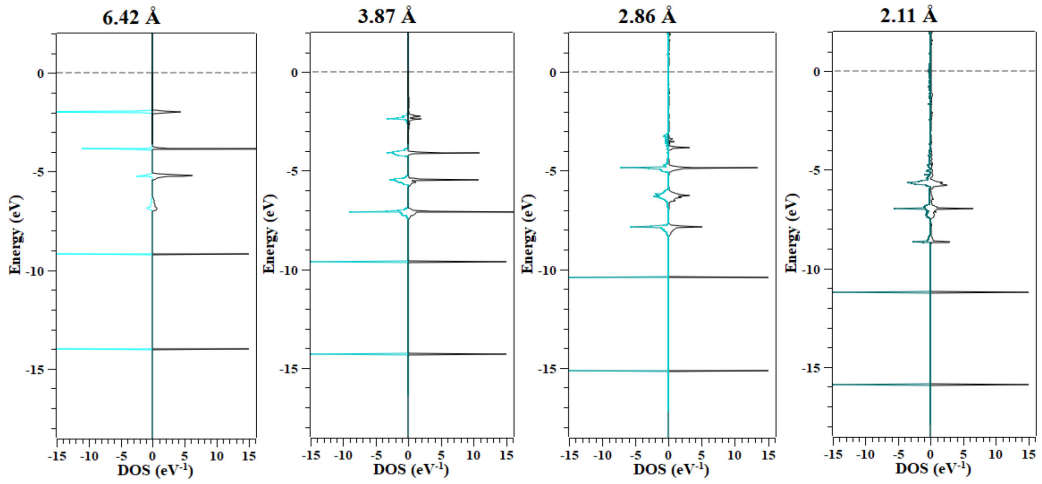

Appendix B-6. Partial DOS of ethylene progressively approaching the surface of Co_{ferro}.

Co_3Mo_{para}

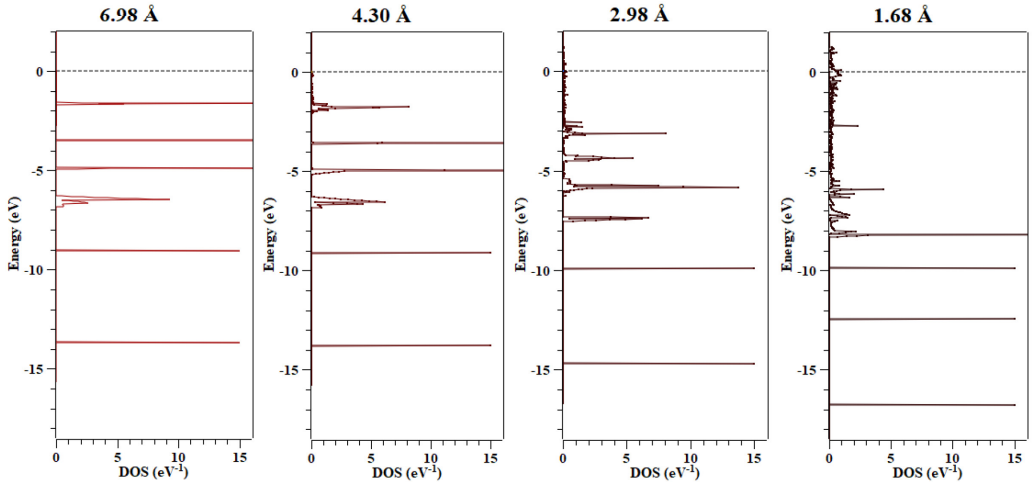

Appendix B-7. Partial DOS of ethylene progressively approaching the surface of Co_3Mo_{para}.

Co_3Mo_{ferro}

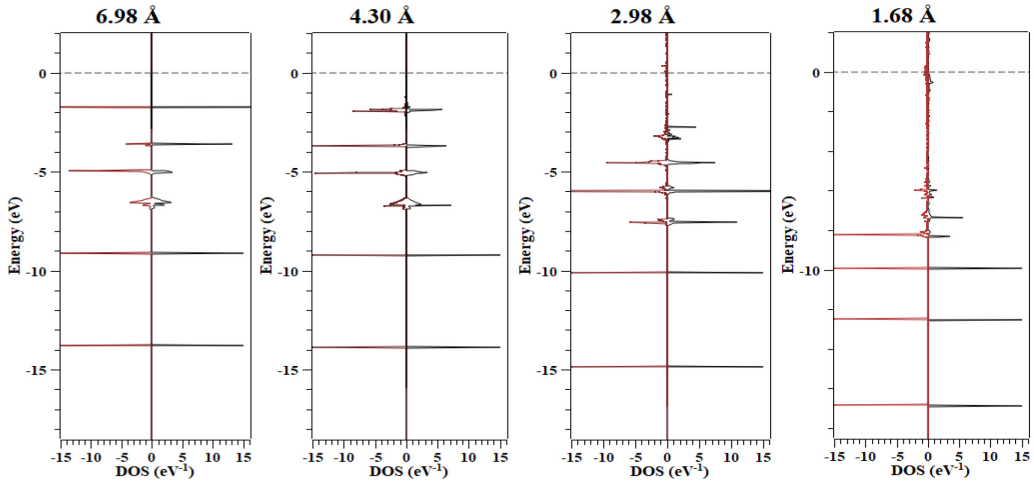

Appendix B-8. Partial DOS of ethylene progressively approaching the surface of Co_3Mo_{ferro}.